TOI-4438 b: a transiting mini-Neptune amenable to atmospheric characterization

Citation for the original published paper (version of record):

Goffo, E., Chaturvedi, P., Murgas, F. et al (2024). TOI-4438 b: a transiting mini-Neptune amenable to atmospheric characterization. Astronomy and Astrophysics, 685.
http://dx.doi.org/10.1051/0004-6361/202349133

A&A, 685, A147 (2024)
https://doi.org/10.1051/0004-6361/202349133

Astronomy & Astrophysics

TOI-4438 b: a transiting mini-Neptune amenable to atmospheric characterization

E. Goffo[1,2], P. Chaturvedi[2], F. Murgas[3,4], G. Morello[5,3,7], J. Orell-Miquel[3,4], L. Acuña[6], L. Peña-Moñino[7], E. Pallé[3,4], A. P. Hatzes[2], S. Geraldía-González[3,4], F. J. Pozuelos[7], A. F. Lanza[8], D. Gandolfi[1], J. A. Caballero[9], M. Schlecker[10], M. Pérez-Torres[7,29,30], N. Lodieu[3,4], A. Schweitzer[11], C. Hellier[12], S. V. Jeffers[13], C. Duque-Arribas[14], C. Cifuentes[9], V. J. S. Béjar[3,4], M. Daspute[15], F. Dubois[16,17], S. Dufoer[16], E. Esparza-Borges[3,4], A. Fukui[18,3], Y. Hayashi[19], E. Herrero[20], M. Mori[19], N. Narita[18,21,3], H. Parviainen[3,4], L. Tal-Or[15], S. Vanaverbeke[16,17,22], I. Hermelo[23], P. J. Amado[7], S. Dreizler[24], Th. Henning[6], J. Lillo-Box[9], R. Luque[25,7], M. Mallorquín[3,4], E. Nagel[24], A. Quirrenbach[26], S. Reffert[26], A. Reiners[24], I. Ribas[20,27], P. Schöfer[7], H. M. Tabernero[14,28], and M. Zechmeister[24]

(Affiliations can be found after the references)

Received 29 December 2023 / Accepted 4 March 2024

ABSTRACT

We report the confirmation and mass determination of a mini-Neptune transiting the M3.5 V star TOI-4438 (G 182-34) every 7.44 days. A transit signal was detected with NASA's TESS space mission in the sectors 40, 52, and 53. In order to validate the planet TOI-4438 b and to determine the system properties, we combined TESS data with high-precision radial velocity measurements from the CARMENES spectrograph, spanning almost one year, and ground-based transit photometry. We found that TOI-4438 b has a radius of $R_\mathrm{b} = 2.52 \pm 0.13\,R_\oplus$ (5% precision), which together with a mass of $M_\mathrm{b} = 5.4 \pm 1.1\ M_\oplus$ (20% precision), results in a bulk density of $\rho_\mathrm{b} = 1.85^{+0.51}_{-0.44}\,\mathrm{g\,cm^{-3}}$ (~28% precision), aligning the discovery with a volatile-rich planet. Our interior structure retrieval with a pure water envelope yields a minimum water mass fraction of 46% (1σ). TOI-4438 b is a volatile-rich mini-Neptune with likely H/He mixed with molecules, such as water, CO_2, and CH_4. The primary star has a J-band magnitude of 9.7, and the planet has a high transmission spectroscopy metric (TSM) of 136 ± 13. Taking into account the relatively warm equilibrium temperature of $T_\mathrm{eq} = 435 \pm 15$ K, and the low activity level of its host star, TOI-4438 b is one of the most promising mini-Neptunes around an M dwarf for transmission spectroscopy studies.

Key words. techniques: photometric – techniques: radial velocities – planets and satellites: composition – planets and satellites: detection

1. Introduction

Precise and accurate planetary mass and radius measurements are necessary to enable the atmospheric characterization of exoplanets. Current and forthcoming telescopes such as the *James Webb* Space Telescope (JWST), the Atmospheric Remote-sensing Infrared Exoplanet Large-survey (Ariel), and the Extremely Large Telescope ELT will expand our frontiers of planetary science, allowing us to explore the composition of the upper gaseous layer of exoplanets. Selecting the best targets amenable to future atmospheric characterization is therefore crucial.

Since the beginning of this century, the CoRoT (Baglin et al. 2006), *Kepler* (Borucki et al. 2010), K2 (Howell et al. 2014), and TESS (Ricker et al. 2015) space-based telescopes have opened our eyes to several thousands of transiting exoplanets in our galaxy. Surprisingly, most of these planets have no counterparts within our solar system, since their sizes are between the ones of Earth and Neptune ($1.0 \lesssim R_\mathrm{p} \lesssim 4.0\,R_\oplus$; Batalha et al. 2013). Small planets with radii $1.8 \lesssim R_\mathrm{p} \lesssim 4.0\,R_\oplus$, the so-called mini-Neptunes, seem to host hydrogen-dominated atmospheres. The composition of the outer atmosphere as well as the internal planetary structure are still not well understood, as they could be explained by several degenerate models (Zeng et al. 2019). Atmospheric follow-up observations are needed to solve the discrepancy between various composition models. With the methodology proposed by Kempton et al. (2018), one can calculate the expected signal-to-noise ratio (S/N) of transmission spectra for a transiting planet, based on the strength of spectral features and the brightness of the host star, assuming cloud-free atmospheres, namely the transmission spectroscopy metric (TSM). The TSM is used for determining which transiting exoplanets are the best targets for atmospheric characterization via transmission spectroscopy, especially with the Near Infrared Imager and Slitless Spectrograph (NIRISS) on JWST.

Small planets including mini-Neptunes happen to be common around M-type dwarf stars (Dressing & Charbonneau 2013; Sabotta et al. 2021; Ribas et al. 2023), as found also in data from the TESS mission (Chaturvedi et al. 2022; Espinoza et al. 2022; Kawauchi et al. 2022; González-Álvarez et al. 2023; Barkaoui et al. 2023). Follow-up observations focused on M dwarfs have their own advantages as these are abundant compared to F, G, and K stars. Their smaller stellar radii and masses produce deeper transit signals (the transit depth δ is inversely proportional to $R_\star^2$) and larger Doppler reflex motions (the radial velocity semi-amplitude $K_\star$ is inversely proportional to $M_\star^{2/3}$), increasing

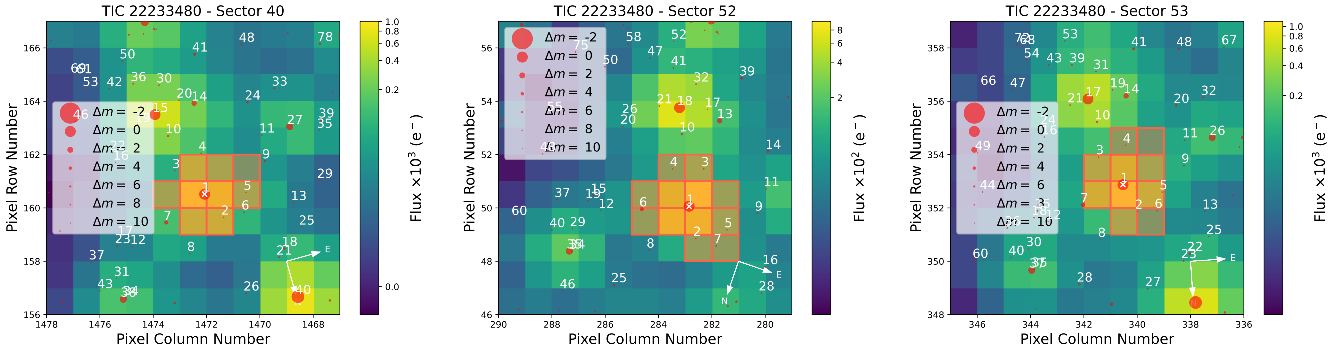

Fig. 1. TPFs of TOI-4438 in TESS sectors 40, 52, and 53. The red bordered squares mark the optimal photometric aperture used to extract the SAP fluxes. The different sizes of the red circles show the *G*-band magnitudes from *Gaia* DR3 for all nearby stars with respect to TOI-4438 (marked with an "×") up to $\Delta G = 10$ mag fainter.

our capability to detect small low-mass planets (see, e.g., Ribas et al. 2023).

Here, we present the characterisation of TESS object of interest (TOI)-4438 b, a transiting mini-Neptune orbiting the M3.5 V star TOI-4438 (G 182-34). We used CARMENES precise radial velocities (RVs) and ground-based transit observations to confirm the planet and to derive its fundamental parameters, such as mass, radius, orbital period, semi-major axis, and equilibrium temperature. TOI-4438 b with a score of ~136 scales very high on TSM, thereby, making it a promising target for future atmospheric observations with JWST. This work is part of the TESS follow-up program within the CARMENES observations survey (see, e.g., González-Álvarez et al. 2023; Kossakowski et al. 2023; Mallorquín et al. 2023; Murgas et al. 2023; Palle et al. 2023).

2. Observations

2.1. TESS photometry

TESS observed TOI-4438 in sector 40, from 25 June to 23 July 2021, with CCD#2 of camera 1 with an integration time of 2 min. TOI-4438 had more observations taken in sector 52, from 19 May to 12 June 2022, and in sector 53, from 13 June to 8 July 2022. The observations were done again at the same cadence of 2 min with CCD#1 of camera 1 in sector 52, and with CCD#2 of camera 1 in sector 53. We retrieved the TESS data from the Mikulski Archive for Space Telescopes (MAST)[1] The data were processed by Science Processing Operations Center (SPOC, Jenkins et al. 2016) pipeline using the Presearch Data Conditioning Simple Aperture Photometry (PDCSAP) algorithm. For details, refer Stumpe et al. (2012, 2014); Smith et al. (2012).

In order to correct for the photometric contamination caused by TESS's large pixel size of 21″, a photometric mask is used to extract the TESS Simple Aperture Photometry (SAP) light curve. We plotted the target pixel files (TPFs; Fig. 1) of TOI-4438 using the code `tpfplotter`[2] (Aller et al. 2020). The TPFs include all the *Gaia* Data Release 3 (DR3, Gaia Collaboration 2023) sources, down to $\Delta G = 10$ mag fainter than the target star and spatially located within the field of view of the TESS aperture. No bright sources fall inside the photometric aperture of TOI-4438. For the analysis presented in this paper, we used the TESS contamination corrected PDCSAP light curves (Fig. 2).

2.2. CARMENES radial velocity follow-up

We spectroscopically monitored TOI-4438 with the Calar Alto high-Resolution search for M dwarfs with Exoearths with Near-infrared and optical Echelle Spectrographs (CARMENES) installed at the 3.5 m telescope at Calar Alto Observatory, Almería, Spain. The instrument comprises two highly stable, fiber-fed spectrographs (Quirrenbach et al. 2014, 2018), one covering the wavelength range 520–960 nm (VIS) with a resolving power of $R \approx 94\,600$, the other covering the near-infrared range 960–1710 nm (NIR), with a resolving power of $R \approx 80\,400$.

We collected 34 high-resolution spectra between 21 May 2022 and 2 May 2023. Depending on the sky condition and observing constraints, each of the spectra was exposed between 700 and 1800 s. The resultant average S/N was ~47 at 740 nm. We followed the standard `caracal` pipeline (Zechmeister et al. 2014) to reduce the CARMENES data.

The precise relative RVs were computed using the `serval`[3] pipeline (Zechmeister et al. 2018) with the standard corrections for barycentric and secular motions. The ancillary corrections applied for the nightly drift by incorporating the nightly zero-points and the atmospheric effects using the telluric lines are described by Nagel et al. (2023). In our analysis we also used the `serval` produced spectral activity indicators, namely, the chromatic index (CRX), the differential line width (dLW), the Hα index, the Ca II infrared triplet (IRT) index, and the Na I D doublet index.

We discarded two data points in the CARMENES VIS RV time series due to their low signal-to-noise ratio ($S/N < 21$). The final CARMENES dataset includes 32 measurements with a root mean square (RMS) of $\approx 2\,\mathrm{m\,s^{-1}}$. We did not include the NIR RVs in our further analysis, given their low S/N. Table A.1 lists the CARMENES VIS RV measurements with the time information in the Barycentric Julian Date- Barycentric Dynamical Time ($\mathrm{BJD_{TDB}}$) units.

2.3. Ground-based photometry

2.3.1. MuSCAT2

TOI-4438 was observed on three nights, namely, on 17 May 2022, 2 May 2023, and 8 July 2023, with the multi-band imager MuSCAT2 (Narita et al. 2019) mounted on the 1.5 m Telescopio *Carlos Sánchez* (TCS) at Teide Observatory, Tenerife, Spain. MUSCAT2 is equipped with four 1k×1k pixel CCDS, with each having a field of view of 7.4′×7.4′. The cameras

---

[1] https://mast.stsci.edu/portal/Mashup/Clients/Mast/Portal.html

[2] https://github.com/jlillo/tpfplotter

[3] https://github.com/mzechmeister/serval

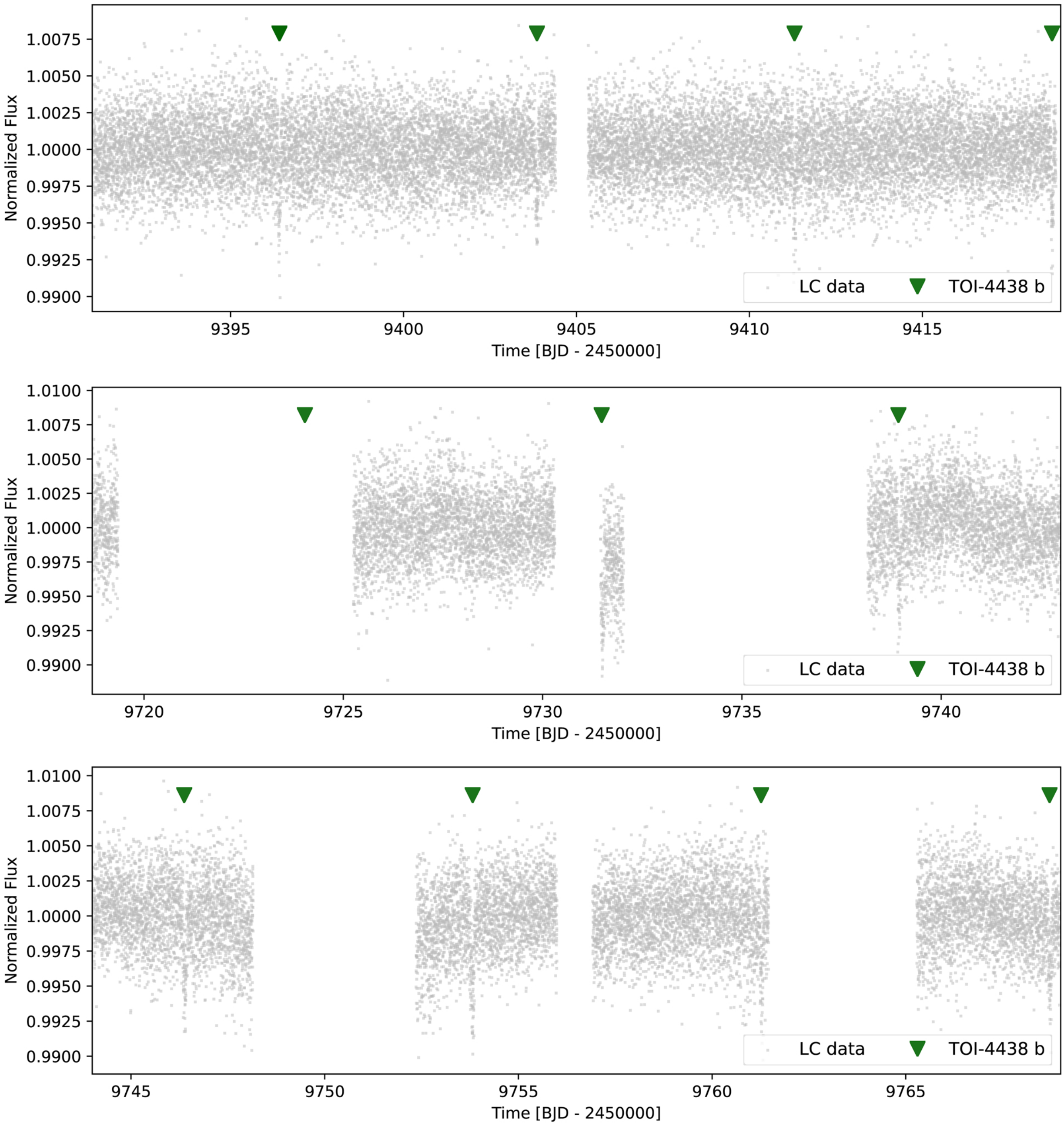

Fig. 2. TESS PDCSAP light curve of TOI-4438 from sectors 40, 52, and 53. The green triangles mark the timings of the transits of TOI-4438 b.

can simultaneously observe in the g', r', i', and z_s bands. We observed two complete transits and one partial transit of TOI-4438 b in each band. The times for exposure varied between 10 s to 30 s. The data reduction were carried out using the standard pipeline as described by Parviainen et al. (2019); Parviainen (2015).

2.3.2. SuperWASP

The SuperWASP transit search (Pollacco et al. 2006) observed the field of TOI-4438 in 2004 and then every year from 2007 to 2010. The eight cameras have each 2048×2048 CCDs with $f/1.8$ lenses. A total of 71 000 photometric data points were obtained over a period of ~120 nights in the visible passband of 400–700 nm. At $V = 13.7$ mag, TOI-4438 is relatively faint for WASP, though it is the brightest star in the 48″ extraction aperture.

2.3.3. TJO

We carried out a dedicated photometry monitoring campaign of TOI-4438 on 49 different nights from April to September 2023 with the 0.8 m Telescopi *Joan Oró* (TJO; Colomé et al. 2010) at the Montsec Observatory, Lleida, Spain. A total of 285 data points were observed using the Johnson R filter of the LAIA imager on a 4k×4k CCD with a 30′ field of view. The standard reduction process was followed using the `AstroImageJ` (Collins et al. 2017) package and the `icat` pipeline (Colome & Ribas 2006) of the TJO. We used indigenous pipelines for removal of outliers for observations made during poor sky conditions. We obtained an effective rms of ~9 ppt in the R filter.

2.3.4. LCOGT

We performed photometric monitoring of TOI-4438 in the V band between 2 August and 6 November 2023, using the

SBIG camera of one of the 40 cm telescope of Las Cumbres Observatory Global Telescope (LCOGT; Brown et al. 2013) providing a field of view of 29.2′×19.5′. We took three exposures of 600 s in each of the 71 different observing epochs during 96 d. The observing conditions were mostly good and the average seeing varied from 2.0 to 6.0″. Raw data were processed using the `BANZAI` pipeline (McCully et al. 2018) and differential aperture photometry of TOI-4438 was performed using the `AstroImageJ` software. An optimal aperture of 8 pixels (∼4.5″) was adopted to minimize the dispersion of the differential light curves.

We used the 1 m LCOGT telescopes from 9 June to 4 November 2023, to observe TOI-4438 in the B filter with an exposure time of 120 s until JD = 2460156, and of 77 s afterwards. This produced 88 images, out of which nine were found to be bad. The final light curve has an rms of 0.57% ∼ with 79 data points, spanning 148 days.

2.3.5. ASAS-SN

TOI-4438 was photometrically monitored by the All-Sky Automated Survey for Supernovae (ASAS-SN; Shappee et al. 2014; Kochanek et al. 2017). ASAS-SN consists of a network of 24 robotic telescopes with a diameter of 14 cm, distributed around the world. We retrieved the ASAS-SN light curve from the webpage of the project[4]. There are 246 V-band photometry measurements taken for the star between 3 May 2013 and 25 September 2018 with a rms scatter of ∼0.021 mag.

2.3.6. e-EYE

TOI-4438 was also observed by e-EYE (Entre Encinas y Estrellas) 16″ ODK corrected-Dall-Kirkham reflector, located at Fregenal de la Sierra in Badajoz, Spain. V band observations were taken between 12 September and 13 November 2023 with a Kodak KAF-16803 CCD chip mounted on ASA DDM85. The images were reduced using the `LesvePhotometry` package[5]. The rms of the data was ∼0.006 mag.

2.3.7. ADONIS

TOI-4438 was observed by the privately owned ADONIS observatory in the V filter from 30 September to 6 December 2023. The telescope used is 0.25 m skywatcher Quattro Newtonian telescope with a Moravian CCD camera. `LesvePhotometry` is used to perform the aperture photometry.

3. Stellar properties

The star TOI-4438 was originally discovered as a high-proper motion star (34th in the plate 182 in Hercules) in the northern hemisphere at the Lowell Observatory by Giclas (1966). The star has been identified as G 182-34 (Giclas et al. 1971) and has been tabulated by a number of catalogs on proper motion (Luyten 1979; Lépine & Shara 2005; Schneider et al. 2016), parallax (Dahn et al. 1988, 2002; van Altena et al. 1995), or the solar neighborhood (Reid & Cruz 2002; Lépine & Gaidos 2011; Frith et al. 2013; Gaia Collaboration 2021).

Table 1. Stellar parameters of TOI-4438.

Parameter	Value	Reference
Identifiers	G 182-34	Gic71
	Karmn J18012+355	Cab16
	TIC 22233480	TIC
Sp. type	M3.5 V	Reid03
α (ICRS, epoch 2016.0)	18:01:16.14	*Gaia* DR3
δ (ICRS, epoch 2016.0)	+35:35:41.6	*Gaia* DR3
$\mu_\alpha \cos\delta$ (mas yr^{-1})	+29.212 ± 0.017	*Gaia* DR3
μ_δ (mas yr^{-1})	–517.512 ± 0.018	*Gaia* DR3
ϖ (mas)	33.2642 ± 0.0154	*Gaia* DR3
d (pc)	30.0623 ± 0.0139	*Gaia* DR3
γ (km s^{-1})	–35.81 ± 0.47	*Gaia* DR3
$T_{\rm eff}$ (K)	3422 ± 81	This work
$\log g_\star$ (cgs)	4.68 ± 0.04	This work
[Fe/H] (dex)	–0.19 ± 0.05	This work
$L_\star$ ($L_\odot$)	0.01706 ± 0.00007	This work
$R_\star$ ($R_\odot$)	0.372 ± 0.018	This work
$M_\star$ ($M_\odot$)	0.368 ± 0.021	This work
$\rho_\star$ (g cm^{-3})	10.06 ± 1.62	This work
$v \sin i_\star$ (km s^{-1})	<2	This work
$P_{\rm rot}$ (days)	68 ± 6	This work
Age (Gyr)	5.1 ± 2.8	This work
G (mag)	12.50 ± 0.68	*Gaia* DR3
T (mag)	11.2695 ± 0.0073	TIC
J (mag)	9.695 ± 0.021	2MASS
K_s (mag)	8.869 ± 0.018	2MASS

References. Gic71: Giclas et al. (1971); Cab16: Caballero et al. (2016); TIC: Stassun et al. (2019); *Gaia* DR3: Gaia Collaboration (2023); 2MASS: Skrutskie et al. (2006); Reid03: Reid et al. (2003).

3.1. Stellar parameters

We derived the stellar parameters as discussed in Schweitzer et al. (2019). The total luminosity was computed by summing over the spectral energy distribution with `VOSA` (Bayo et al. 2008). Broadband photometry from passbands Johnson (B) to AllWISE ($W4$) and astrometry from *Gaia* DR3 catalog were utilized. The stellar atmospheric parameters ($T_{\rm eff}$, $\log g$, and [Fe/H]) were derived with the `SteParSyn`[6] code (Tabernero et al. 2022) using the line list and model grid described by Marfil et al. (2021). The mass of the star was derived using the linear mass-radius relation (Schweitzer et al. 2019) whereas the radius of the star was derived from Stefan-Boltzmann's law assuming the bolometric luminosity and the spectroscopic temperature. The stellar parameters of TOI-4438 are listed in Table 1. The effective temperature of $T_{\rm eff} = 3422 \pm 81$ K and surface gravity of $\log g_\star = 4.68 \pm 0.04$ (cgs) match the ∼M3 V spectral-type from the spectro-photometric relations of Pecaut & Mamajek (2013) and Cifuentes et al. (2020) and, the M3.5±0.5 V spectral type from low-resolution optical spectroscopy by Reid et al. (2003).

3.2. Stellar activity

The broad wavelength range coverage offered by the CARMENES VIS and NIR channels allows us to study a total of sixteen spectral activity indicators. These are pEW(Hα)

---

[4] https://asas-sn.osu.edu/

[5] www.dppobservatory.net

[6] https://github.com/hmtabernero/SteParSyn/

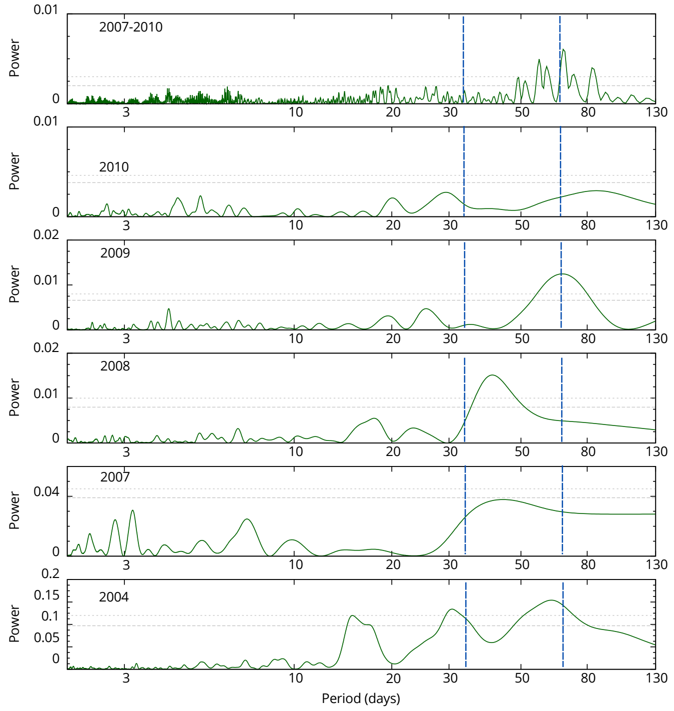

Fig. 3. Periodogram of the SuperWASP data for TOI-4438 from each year and (*top*) the periodogram of 2007–2010 combined. The horizontal dashed lines indicate the estimated 10%- and 1%-likelihood false-alarm levels. The blue vertical dashed lines mark the stellar rotation period and its first harmonic.

(from which we derived $\log \mathrm{H}\alpha/L_{\mathrm{bol}}$ as Jeffers et al. 2018), HeD3, NaD, Ca IRT-a,-b,-c, He Iλ10830, Pa β, CaH2, CaH3, TiO 7050, TiO 8430, TiO 8860, VO 7436, VO 7942, and FeH Wing-Ford, and they were computed following the methods described by Schöfer et al. (2019). In addition, the output parameters from `serval` also include the CRX and dLW parameters for both channels (Zechmeister et al. 2018), resulting in twenty activity diagnostics.

In all CARMENES spectra we found that Hα is in absorption, indicating that TOI-4438 is a weakly active star with undetectable levels of activity-induced emission in the Hα line. We also did not detect Hα emission due to flaring in the CARMENES spectra. Jeffers et al. (2018) showed that only about one third of M3 dwarfs are Hα active. Given the M3.5 V spectral type, the low activity level of TOI-4438 is therefore not surprising. We also computed Pearson's r correlation coefficient between the measured RVs and the spectral activity indicators as described in Jeffers et al. (2020) and confirmed the star to be least active.

3.3. Rotation period of the star

We inspected the SuperWASP light curves for rotational modulations as discussed in Maxted et al. (2011). There appears to be significant power at long periods (see Fig. 3), although the periodograms are hard to interpret. In each observation season, the amplitude of the modulations is variable, and the data covered only about two cycles. There are likely to be profile and phase changes between years. We found a rotational modulation with an amplitude of ∼6 mag, and a period of 68 ± 6 d. The first harmonic is also present at ∼34 days in the years 2004 and 2010.

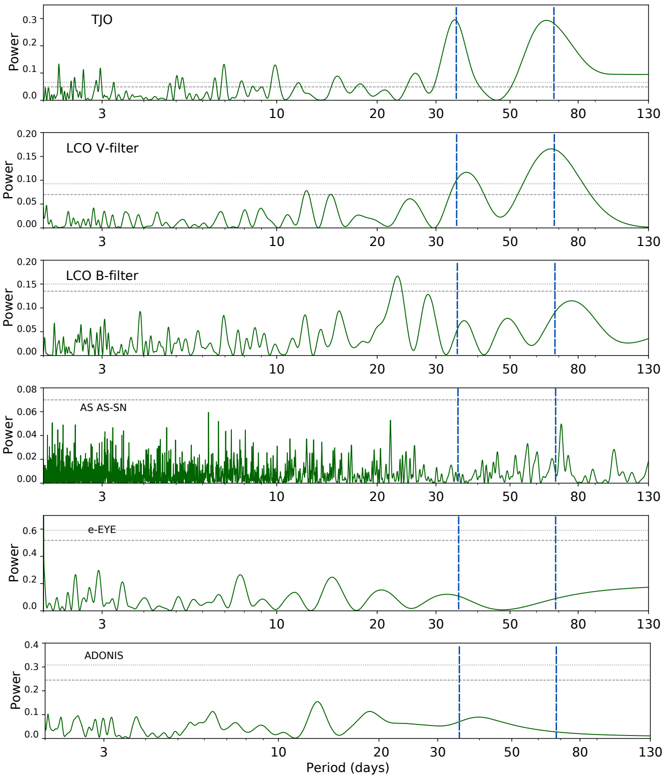

Fig. 4. Periodograms of the TJO, LCOGT (*V* and *B*), ASAS-SN, e-EYE, and ADONIS data for TOI-4438. The horizontal dashed lines indicate the estimated 10%- and 1%-likelihood false-alarm levels. The blue vertical dashed lines mark the stellar rotation period and its first harmonic.

In addition, we computed the generalized Lomb-Scargle (GLS; Zechmeister & Kürster 2009) periodograms of the TJO, LCOGT (in *V*- and *B*- filters), ASAS-SN, e-EYE, and ADONIS light curves of TOI-4438, as shown in Fig. 4. The periodogram of the TJO light curve shows its highest peak at ∼34 d, and a second high peak at ∼64 days, consistent with the SuperWASP results. The same applies to the periodogram of the LCOGT data (*V*-filter), where we found the highest signal at 68 ± 10 d, and the ASAS-SN photometry, which shows a modulation at around 57 d. LCOGT *B*-filter data show a peak at 22 ± 1 days with a false alarm probability of <0.1%, which could be related to the second harmonic of the stellar rotation period. Since the e-EYE and ADONIS data covered a shorter baseline, the periodograms displayed no significant signals around 68 or 34 days. We concluded that TOI-4438 has a rotation period of 68 ± 6 days, as derived from SuperWASP photometry.

3.4. Age

With a rotation period of 68 ± 6 days, TOI-4438 is very likely an old star. From the relations of Bouma et al. (2023), a maximum rotation period of 25 days is detected for members of the Praesepe cluster (500–700 Myr; Lodieu et al. 2019). The rotation period of TOI-4438 is at least twice longer, so the age is expected to be much older, although the relation is not linear. Similarly, Curtis et al. (2020) showed that field stars with spectral types between K0 and M1–M2 and ages of 6 ± 2 Gyr have rotation periods around 35–45 d, again much shorter than TOI-4438. Eventually, we used the rotation–age relations applicable to M2.5–6.5 dwarfs from the recent study by Engle & Guinan (2023) and derived an age of 5.1 ± 2.8 Gyr.

To constrain the age of an M-type dwarf we can also look for wide, higher-mass, gravitationally bound companions. We searched for possible co-moving common proper motion companions to TOI-4438 in the *Gaia* Data Release 3 (DR3) in a radius of five degrees. The search was based on the proximity in parallax, using a very conservative interval of 3.25 pc, 200 times more than the error bar on the parallax reported in DR3. Ten sources were returned but none of them shows a proper motion in right ascension consistent with the large motion of TOI-4438 ($\mu_\alpha \cos\delta \approx -517.5$ mas yr^{-1}). Moreover, we checked several parameters that may indicate departure from a single star astrometric model, such as the renormalized unit weight error (RUWE), the excess noise of the source and its significance, and the percent of successful-IPD windows with more than one peak. None of them point toward the presence of an unseen companion around TOI-4438. This is consistent with the null results on TOI-4438 of the laser-guided, adaptive-optics, Robo-AO M-dwarf multiplicity survey of Lamman et al. (2020).

4. Analysis

4.1. Transit light curve modeling

Prior to performing a joint analysis of the photometric and Doppler time series (Sect. 4.4), we performed a preliminary analysis of the available transit light curves to check whether the different passbands provide consistent transit depths. With this aim, we used the code `pyaneti` (Barragán et al. 2019, 2022) to model the TESS light curve from sectors 40, 52, and 53 (Sect. 2.1), and MuSCAT2 ground-based photometry (Sect. 2.3.1). The TESS data included in the analysis are subsets of 8 h of the PDCSAP light curves, centered around each transit epoch, and detrended by fitting a second-order polynomial to the out-of-transit data.

Based on the period and ephemeris reported by SPOC ($P_{\mathrm{orb,b}} = 7.446303 \pm 0.000023$ days and $T_{0,\mathrm{b}} = 2459396.40958 \pm 0.00075$ BJD$_{\mathrm{TDB}}$), we allowed the period to vary between 7.2 and 7.7 d, and the epoch of reference transit between BJD$_{\mathrm{TDB}}$ = 2459396.16 and 2459396.66 days. We adopted the parameterization proposed by Anderson et al. (2010) for the eccentricity e and the argument of periastron of the stellar orbit $\omega_\star$ (i.e., $\sqrt{e}\sin\omega_\star$ and $\sqrt{e}\cos\omega_\star$). `pyaneti` uses Mandel & Agol (2002)'s limb-darkened quadratic model for the transit light curve and the limb-darkening parameterization proposed by Kipping (2013). We adopted Gaussian priors for the linear and quadratic limb-darkening coefficients (q_1, q_2) using the values calculated with the `Python Limb Darkening Toolkit`[7] (PyLDTk, Parviainen & Aigrain 2015) for TESS and MuSCAT2 bands. We set uniform priors for all of the remaining parameters. A photometric jitter term was added to account for any instrumental noise not included in the nominal uncertainties. We sampled the parameter space with 500 walkers using the Markov chain Monte Carlo (MCMC) ensemble sampler algorithm implemented in `pyaneti`. We created the posterior distributions using the last 5000 iterations of the converged chains with a thin factor of 10, giving a distribution of 250 000 data points for each sampled parameter. We followed the procedure and the convergence test as described by Barragán et al. (2019).

In order to check for uniform transit depths in the TESS and MuSCAT2 bands, and determine the chromaticity of the transits in each available filter, we performed two analyses: (1) we allowed an independent scaled planetary radius $R_{\mathrm{b}}/R_\star$ for each passband; (2) we modeled a single scaled planetary radius, namely assuming the same transit depth in all passbands. Table 2 lists the adopted priors and posterior values of the sampled parameters. For the parameter estimates and their 1σ uncertainties, we took the median and the 68.3% credibility interval of the posterior distributions. Figure 5 shows the phase-folded TESS and MuSCAT2 transit light curves of TOI-4438 b. We measured an orbital period of $P_{\mathrm{orb,b}} = 7.4462800 \pm 0.0000087$ days, an epoch of reference transit of $T_{0,\mathrm{b}} = 2459396.4116 \pm 0.0006$ days (BJD$_{\mathrm{TDB}}$), and a radius of $R_{\mathrm{b}} = 2.51 \pm 0.12\,R_\oplus$ from the unique scaled planet radius fit (case 2).

Figure 6 displays the posterior distributions for the sampled scaled planetary radii $R_{\mathrm{p}}/R_\star$ for each passband. We found that the posterior distributions for the TESS and MuSCAT2 bands overlap, except for the g' and r' filters.

We also found a color dependence, given the deeper transits in the g' and r' filters. Assuming an astrophysical origin, this color trend could be caused by contamination from a cooler dwarf (Parviainen et al. 2019) or unocculted star spots (Ballerini et al. 2012). Potential inaccuracies due to the stellar limb-darkening parameterization (Morello et al. 2017) or planetary atmospheric signatures (Chen et al. 2021) should be negligible compared to the error bars. In order to check the hypothesis of astrophysical contamination, we fitted the measured planetary radii in multiple bands by assuming a unique planet-to-star radius ratio $R_{\mathrm{b}}/R_\star$ and different star spots configurations modeled with `ExoTETHyS` (Morello et al. 2021). The stellar spectrum was modeled as the sum of two components, namely the quiet photosphere and the spots, characterized by different values of T_{eff} and $\log g_\star$, and neglecting stellar limb-darkening effects (Cracchiolo et al. 2021; Thompson et al. 2023). We adopted the `PHOENIX-COND` and `PHOENIX-DRIFT` libraries of stellar spectra (Claret et al. 2012, 2013; Husser et al. 2013). Technical details are given in Appendix B. It turned out that a spot filling factor of ~40% and temperature contrast of ~500 K are needed to explain the different measurements between g' and TESS filters, but they struggle to maintain the uniform transit depth observed in i', z_s, and TESS. Furthermore, these values would denote a very high level of stellar activity, in contrast with all other indicators (see Sect. 3.2). This scenario is mathematically equivalent to that of a cooler M-type contaminant with similar brightness to that of the host star, following the model by Morello et al. (2023). Such a bright contaminant is also unlikely to be unseen (see Sect. 3.4). Another possibility is that the transit measurements in g' and r' bands are affected by systematic bias, due to the low S/N of the MuSCAT2 light curves obtained with these filters. Therefore, we ignored the bluer g' and r', and used i' and z_s only for the following analysis. We discuss an alternative solution including all bands and potential color contamination in Appendix B.

4.2. Additional planet search and detection limits

We adopted the box least-square (`BLS`; Kovács et al. 2002; Hartman & Bakos 2016) method to look for additional transits in the PDCSAP TESS light curves. Before applying the BLS we detrended the data using the package `citlalique`[8], which allows to detrend light curves using Gaussian processes (GPs) to remove low frequency signals in the light curves (Barragán et al. 2022).

---

[7] https://github.com/hpparvi/ldtk

[8] https://github.com/oscaribv/citlalicue

Table 2. TOI-4438 b parameters from the transit light curve modeling with `pyaneti`.

Parameter	Prior	Derived value (multi-radii)	Derived value (single radius)
Model parameters			
$P_{\rm orb,b}$ (days)	$\mathcal{U}[7.2, 7.7]$	7.4462801 ± 0.0000091	7.4462800 ± 0.0000087
$T_{0,\rm b}$ (BJD$_{\rm TDB}$−2 450 000)	$\mathcal{U}[9396.16, 9396.66]$	9396.4116 ± 0.0007	9396.4116 ± 0.0006
$R_{\rm b}/R_\star$	$\mathcal{U}[0.001, 0.09]$	...	$0.0619^{+0.0006}_{-0.0005}$
$R_{\rm b}/R_\star$TESS	$\mathcal{U}[0.001, 0.09]$	0.0606 ± 0.0012	...
$R_{\rm b}/R_\star$MuSCAT2 g′	$\mathcal{U}[0.001, 0.09]$	0.0678 ± 0.0026	...
$R_{\rm b}/R_\star$MuSCAT2 r′	$\mathcal{U}[0.001, 0.09]$	0.0661 ± 0.0019	...
$R_{\rm b}/R_\star$MuSCAT2 i′	$\mathcal{U}[0.001, 0.09]$	0.0622 ± 0.0013	...
$R_{\rm b}/R_\star$MuSCAT2 z$_{\rm s}$	$\mathcal{U}[0.001, 0.09]$	0.0624 ± 0.0010	...
$b_{\rm b}$	$\mathcal{U}[0, 1]$	$0.38^{+0.16}_{-0.24}$	$0.15^{+0.14}_{-0.10}$
$a/R_\star$	$\mathcal{U}[1, 50]$	$28.6^{+4.0}_{-4.9}$	30 ± 5
$\sqrt{e_{\rm b}} \sin \omega_{\star,\rm b}$	$\mathcal{U}[-1, 1]$	$-0.13^{+0.38}_{-0.25}$	$-0.14^{+0.40}_{-0.27}$
$\sqrt{e_{\rm b}} \cos \omega_{\star,\rm b}$	$\mathcal{U}[-1, 1]$	-0.004 ± 0.447	-0.02 ± 0.47
Derived parameters			
$R_{\rm b}$ ($R_\oplus$)	...	...	2.51 ± 0.12
$R_{\rm b,TESS}$ ($R_\oplus$)	...	2.46 ± 0.13	...
$R_{\rm b,MuSCAT2\,g'}$ ($R_\oplus$)	...	2.75 ± 0.17	...
$R_{\rm b,MuSCAT2\,r'}$ ($R_\oplus$)	...	2.68 ± 0.15	...
$R_{\rm b,MuSCAT2\,i'}$ ($R_\oplus$)	...	2.52 ± 0.13	...
$R_{\rm b,MuSCAT2\,z_s}$ ($R_\oplus$)	...	2.53 ± 0.13	...
$a_{\rm b}$ (au)	...	$0.0492^{+0.0074}_{-0.0086}$	0.053 ± 0.009
$e_{\rm b}$	...	$0.21^{+0.24}_{-0.14}$	$0.23^{+0.25}_{-0.15}$
$\omega_{\star,\rm b}$ (deg)	...	-34^{+134}_{-111}	-37^{+139}_{-108}
$i_{\rm b}$ (deg)	...	$89.22^{+0.50}_{-0.53}$	$89.71^{+0.35}_{-0.21}$
$\tau_{14,\rm b}$ (h)	...	2.02 ± 0.03	2.01 ± 0.02
$T_{\rm eq,b}$ (K) $^{(a)}$	...	453^{+46}_{-30}	438^{+45}_{-32}
$S_{\rm b}$ ($S_\oplus$)	...	$7.04^{+3.3}_{-1.7}$	$6.1^{+2.9}_{-1.6}$
Additional model parameters			
Parameterized limb-darkening coefficients			
$q_{1,\rm TESS}$	$\mathcal{N}[0.276, 0.1]$	0.30 ± 0.08	0.30 ± 0.08
$q_{2,\rm TESS}$	$\mathcal{N}[0.261, 0.1]$	0.26 ± 0.10	0.26 ± 0.10
$q_{1,\rm MuSCAT2\,g'}$	$\mathcal{N}[0.629, 0.1]$	0.64 ± 0.10	0.64 ± 0.10
$q_{2,\rm MuSCAT2\,g'}$	$\mathcal{N}[0.312, 0.1]$	0.35 ± 0.10	0.35 ± 0.10
$q_{1,\rm MuSCAT2\,r'}$	$\mathcal{N}[0.572, 0.1]$	0.55 ± 0.16	0.55 ± 0.16
$q_{2,\rm MuSCAT2\,r'}$	$\mathcal{N}[0.317, 0.1]$	0.33 ± 0.10	0.33 ± 0.10
$q_{1,\rm MuSCAT2\,i'}$	$\mathcal{N}[0.334, 0.1]$	0.37 ± 0.08	0.37 ± 0.08
$q_{2,\rm MuSCAT2\,i'}$	$\mathcal{N}[0.260, 0.1]$	0.31 ± 0.10	0.31 ± 0.10
$q_{1,\rm MuSCAT2\,z_s}$	$\mathcal{N}[0.241, 0.1]$	0.16 ± 0.08	0.16 ± 0.08
$q_{2,\rm MuSCAT2\,z_s}$	$\mathcal{N}[0.240, 0.1]$	0.19 ± 0.10	0.19 ± 0.10
Jitter terms			
$\sigma_{\rm TESS}$	$\mathcal{J}[0,100]$	0.000058 ± 0.000054	0.000058 ± 0.000054
$\sigma_{MuSCAT2\,g'}$	$\mathcal{J}[0,100]$	0.00021 ± 0.00020	0.00021 ± 0.00020
$\sigma_{\rm MuSCAT2\,r'}$	$\mathcal{J}[0,100]$	0.00030 ± 0.00026	0.00030 ± 0.00026
$\sigma_{\rm MuSCAT2\,i'}$	$\mathcal{J}[0,100]$	0.00014 ± 0.00012	0.00014 ± 0.00012
$\sigma_{\rm MuSCAT2\,z_s}$	$\mathcal{J}[0,100]$	0.00018 ± 0.00026	0.00018 ± 0.00026

Notes. $\mathcal{U}[a, b]$ refers to uniform priors between a and b; $\mathcal{N}[a, b]$ refers to Gaussian priors with mean a and standard deviation b; $\mathcal{J}[a, b]$ refers to Jeffrey's priors between a and b. Inferred parameters and uncertainties are defined as the median and the 68.3% credible interval of their posterior distributions. $^{(a)}$ Assuming zero albedo and uniform redistribution of heat.

We used the `BoxLeastSquares` class of the `astropy.timeseries` python package. Whenever the program identified a transit signal, we removed the in-transit data points and ran the algorithm again to search for additional transiting planets. The BLS periodograms of the TESS light curves were evaluated over periods from 0.5 day to half the total length of the observations, namely ∼190 days. The first transit signal was identified at 7.44 days, corresponding to the orbital period of TOI-4438 b. We found no other signals in the data corresponding to additional transiting planets.

To identify possible additional companions that might perturb the orbit of TOI-4438 b, we analysed the available transit

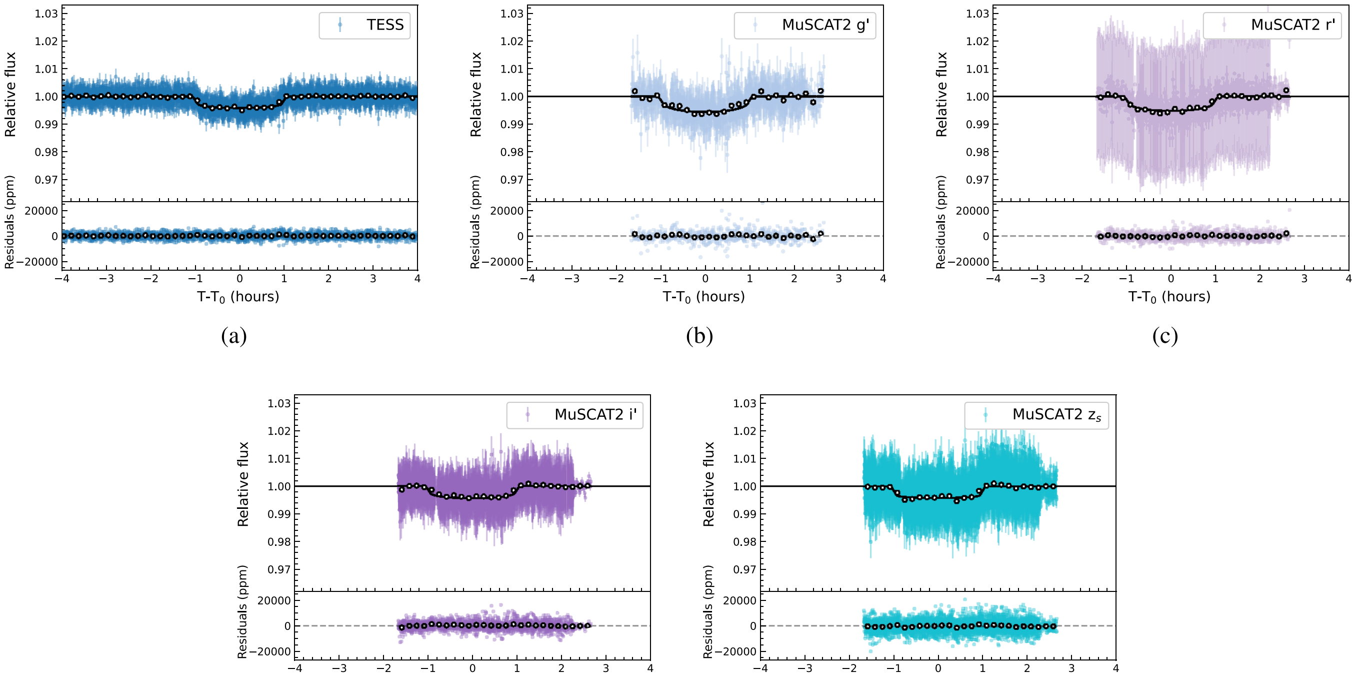

(a) (b) (c)

(d) (e)

Fig. 5. Phase-folded transit light curves of TOI-4438 b from the (*a*) TESS, and (*b*) g', (*c*) r', (*d*) i', and (*e*) z_s MuSCAT2 bands. Data are shown as filled circles with their nominal uncertainties. The 10-min binned data points are marked with white circles.

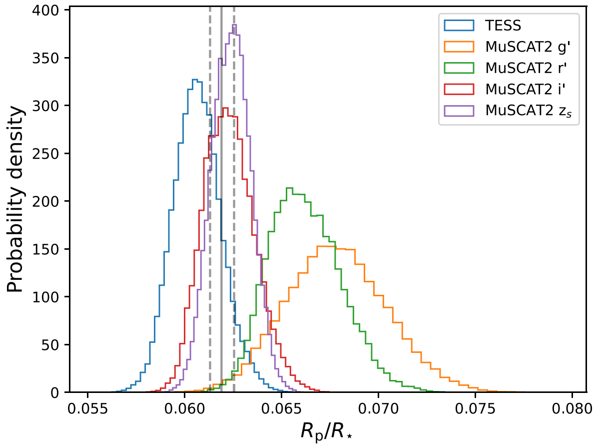

Fig. 6. Posterior distributions of the sampled scaled planetary radii $R_b/R_\star$ for the TESS and MuSCAT2 g', r', i', z_s bands. The solid and dotted, vertical, gray lines mark the median and the 68.3% credibility interval of the $R_p/R_\star$'s posterior distribution, as derived in case 2 (see Sect. 4.1).

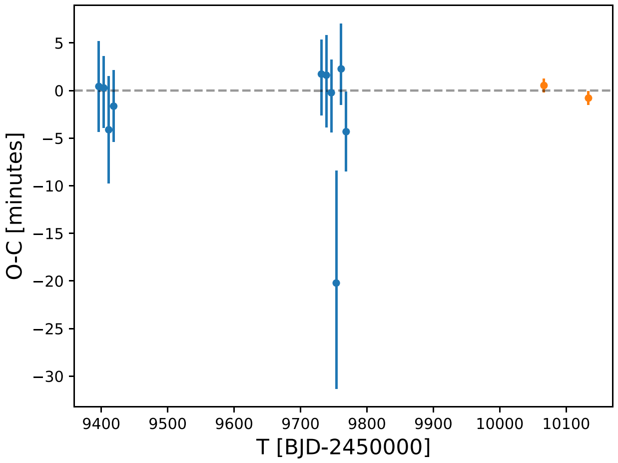

Fig. 7. Transit-timing variations of TOI-4438 b. Blue points correspond to TESS transits while the orange points correspond to the full MuSCAT2 transits.

light curves for transit timing variation (TTVs). We used the ten TESS transits from sectors 40, 52, and 53, and the two full transits observed with MuSCAT2 on 2 May and 8 July 2023. We co-added the data from MuSCAT2 passbands z_s and i' prior to the analysis. We individually modeled the mid-time of each transit with the code `pyaneti` (Barragán et al. 2022). We found no significant TTV in the ~770 days baseline of our observations, as shown in Fig. 7.

The lack of extra signals attributable to transiting planets in the TESS data might be due to one of the following scenarios (see, e.g., Wells et al. 2021; Schanche et al. 2022; Delrez et al. 2022; Pozuelos et al. 2023): (1) no other planets exist in the system; (2) they do exist, but they do not transit; (3) they do exist and transit the host star, but have orbital periods longer than the ones explored in this study; (4) they do exist and transit, but the photometric precision of the data is not high enough to detect them. Scenarios (1) and (2) might be further explored by employing RV follow-up data as discussed in Sect. 2.2. Scenario (3) can be tested when TESS will reobserve TOI-4438 in sectors 79 and 80 (June–July 2024), extending the available time baseline[9]. To evaluate scenario (4), we studied the detection

---

[9] See the TESS-point Web Tool available at `https://heasarc.gsfc.nasa.gov/wsgi-scripts/TESS/TESS-point_Web_Tool/TESS-point_Web_Tool/wtv_v2.0.py/`

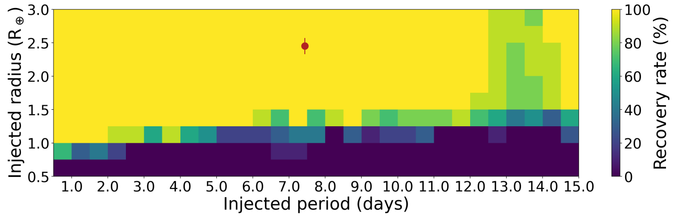

Fig. 8. The resulting detectability map from the injection-and-retrieval experiment. Each pixel corresponds to ten of the 3000 different scenarios, that is, 10 light curves with injected planets having different $P_{\rm planet}$, $R_{\rm planet}$, and T_0. Larger recovery rates are presented in yellow and green colors, while lower recovery rates are shown in blue and darker hues. The red dot refers to TOI-4438 b, which has a recovery rate of 100%, highlighting the ease of detecting mini-Neptunes in this TESS data set with orbital periods shorter than 15 d.

limits of the current TESS photometry conducting injection-and-recovery experiments with the `MATRIX` code[10] (Dévora-Pajares & Pozuelos 2022). We used the `MATRIX` code to inject synthetic planets over the PDCSAP light curves corresponding to the three TESS sectors used in this study, combining a unique set of radius, orbital period, and phase for each synthetic planet. We explored the $R_{\rm planet}$–$P_{\rm planet}$ parameter space in the ranges of 0.5–3.0 $R_\oplus$ with steps of 0.25 $R_\oplus$, and 0.5–15.0 days with steps of 0.25 day. Moreover, for each combination of $R_{\rm planet}$–$P_{\rm planet}$ `MATRIX` produces five different phases, that is, different values of T_0. In total, we explored 3000 scenarios. For simplicity, the injected planets had impact parameters and eccentricities equal to zero.

Once the synthetic planets were injected in `MATRIX`, we detrended the light curves using a bi-weight filter with a window size of 0.5 day, which was found to be the optimal value to recover the known planet TOI-4438 b. Moreover, existing transits in the data were masked out to evaluate the ease of finding TOI-4438 b-like planets. In `MATRIX`, a synthetic planet is recovered when its epoch matches the injected epoch with 1 h accuracy, and its period is within 5% of the injected period. Since we injected the synthetic signals in the PDCSAP light curve, these signals were not affected by the PDCSAP systematic corrections; hence, the detection limits that we found represent the most optimistic scenario (see, e.g., Pozuelos et al. 2020).

The resulting detectability map from this injection-and-retrieval experiment is shown in Fig. 8. On the one hand, we found that transiting Earth- and sub-Earth size planets would remain unnoticed for the complete set of periods explored with recovery rates ranging from 50 to 0%. On the other hand, mini-Neptunes such as TOI-4438 b, seem to be easily detectable, with recovery rates higher than 80% for all the periods, that is, the presence of additional transiting planets in the system with sizes larger than 1.5 $R_\oplus$ and with orbital periods between 0.5 and 15.0 days seems unlikely.

4.3. Frequency analysis of the RV data

We performed a frequency analysis to search for periodic signals due to orbiting planets or stellar activity. We computed the GLS periodograms of the CARMENES RVs and activity indicators, as shown in Fig. 9. We estimated the false alarm probability (FAP) using the bootstrap method as described by Murdoch et al. (1993). We calculated the periodogram of 10^6 time series obtained by randomly shuffling the data and their error bars, keeping the time values fixed. We determined that a peak is significant when it has a FAP < 0.1% (Cochran & Hatzes 1996).

The GLS periodogram of the CARMENES RVs in the VIS band (Fig. 9, upper panel) shows the highest peak at $f_1 = 0.13$ day^{-1}, corresponding to a period of about 7.44 d. This signal is not significant (FAP < 10%) within the frequency range 0.0–0.3 day^{-1}. However, the peak was found at a known frequency, namely the orbital frequency of the planet, providing strong evidence that the signal is related to TOI-4438 b. We estimated the FAP of the peak at orbital frequency of TOI-4438 b using the “windowing bootstrap” method described by Hatzes (2019) and following the procedure done in Osborne et al. (2024). We found a FAP = 0.002% for f_1, which confirms the planetary nature of the signal discovered by TESS.

We also used a pre-whitening technique (Hatzes et al. 2010) to find additional signals. We subtracted the 7.44 days signal from the VIS RVs. The periodogram of the RV residuals following the subtraction of the signal at f_1 (second panel) shows no other significant signal.

Finally, we performed a frequency analysis of the activity indicators obtained using the `serval` pipeline. The GLS periodograms show peaks at periods >30 days, with a FAP > 10% (lower panels of Fig. 9). Although not significant, peaks at ~68 days and ~34 days are present in the periodograms of the CRX, the Ca II IRT2, Hα, and Na I D indices. The peaks appear at the periods observed in the ground-based photometry analysis of Sect. 3.3, corroborating the stellar rotational period, and its first and second harmonic at 68 d, 34 d, and 22 d, respectively.

4.4. Joint fit of the transit light curves and RV measurements

We performed a joint modeling combining TESS, MuSCAT2 i' and z_s transit light curves, and CARMENES VIS RV measurements, following the results presented in Sects. 4.1 and 4.3. We used the code `pyaneti` to perform an MCMC analysis. We followed the procedures described previously in Sect. 4.1, adopting uniform priors for the orbital period and reference transit epoch of TOI-4438 b. We used the same parameterizations and prior distributions as in Sect. 4.1. We performed two analyses: (i) we assumed a circular orbit fixing $\sqrt{e}\sin\omega_\star$ and $\sqrt{e}\cos\omega_\star$ to zero; (ii) we fitted for an eccentric orbit. In a preliminary analysis we used a uniform prior for the stellar density $\rho_\star$. The modeling of the transit light curves gave a mean stellar density consistent with the density of Table 1, which corroborates the planetary nature of the transit signals. We then sampled for the stellar density $\rho_\star$ using a Gaussian prior on the stellar mass and radius, derived in Sect. 3.1, and used wide uniform priors for the remaining model parameters. We fitted for photometric and RV jitter terms to account for possible signals not captured by our models, or instrumental noise not included in the nominal error bars.

We explored the parameter space with 500 Markov chains initialized randomly inside the prior ranges. Once all chains converged, we used the last 5000 iterations of the converged chains with a thin factor of 10 to create the posterior distributions, leading to a distribution of 250 000 data points for each sampled parameter. This procedure ensured a homogeneous sampling of the parameter space. We followed the same procedure and convergence test as described by Barragán et al. (2019).

Results and prior ranges of the fitted and derived parameters are reported in Table 3. Since the planet is not close enough to

---

[10] The `MATRIX` (Multi-phAse Transits Recovery from Injected eXoplanets) code is open access on GitHub at https://github.com/PlanetHunters/tkmatrix

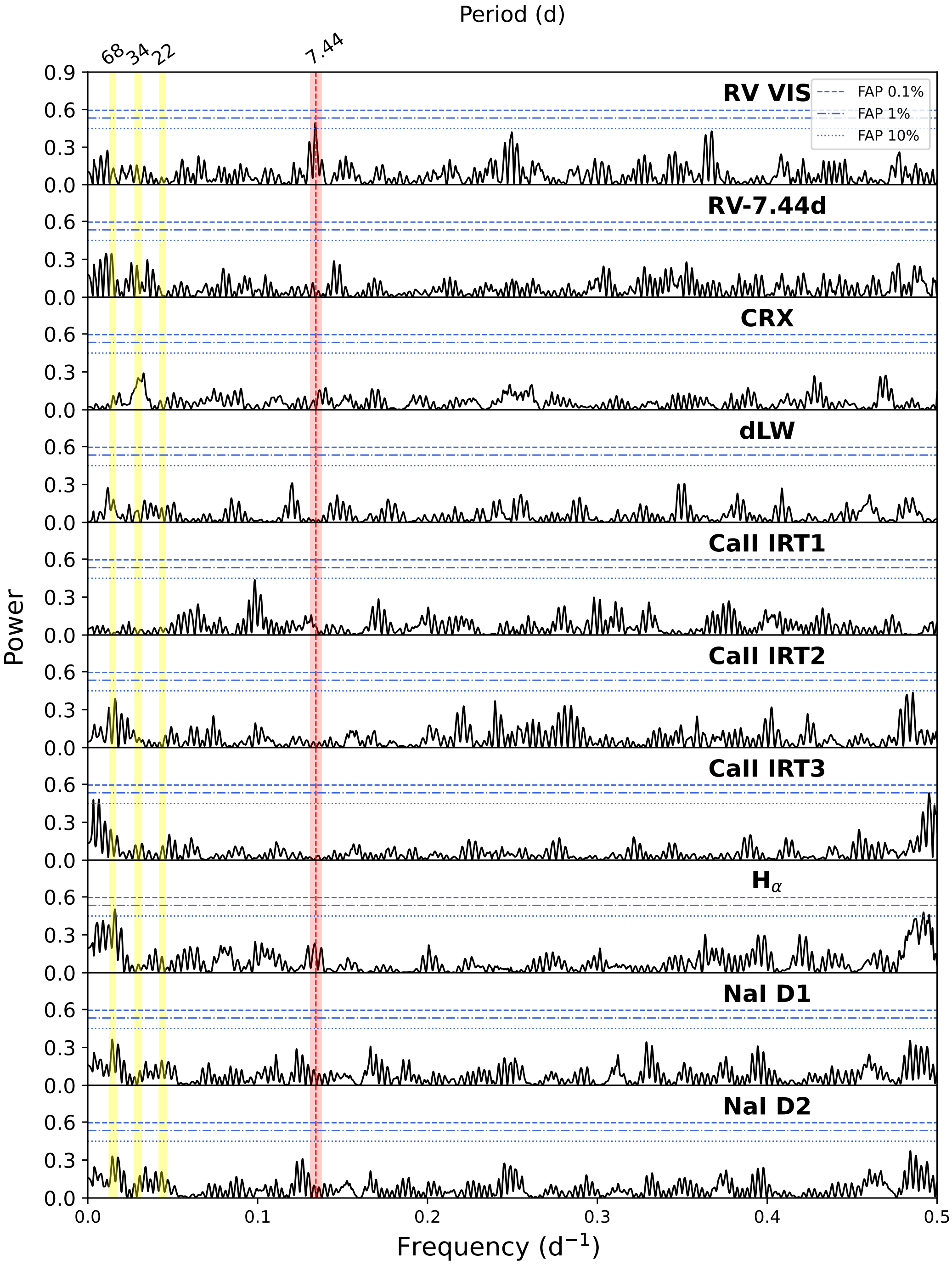

Fig. 9. GLS periodograms of the CARMENES VIS RV measurements (*upper panel*), and RV residuals after subtracting f_1 (*second panel*). The periodograms of the activity indicators are shown in the remaining panels. The 10%, 1%, and 0.1% FAPs are shown with horizontal blue lines. The red vertical line marks the orbital frequency of the transiting planet TOI-4438 b. The yellow vertical lines mark the stellar rotation period at ~68 days, and its first and second harmonics.

the star to expect tidal circularization and there are no other reasons to assume so (Sect. 4.5), we chose the eccentric model as the best-fit, although the resulting eccentricity is consistent with zero.

Figures 10 and 11 display the CARMENES VIS time series and the RV curve phase-folded at the orbital period of TOI-4438 b, respectively, along with the best-fitting Doppler model. We found an RV semi-amplitude variation of $K_b = 3.50 \pm 0.72$ m s^{-1}, and a planetary mass of $M_b = 5.4 \pm 1.1$ $M_\oplus$ (20% precision). We measured a radius of $R_b = 2.52 \pm 0.13\,R_\oplus$ (5% precision). Combining the planetary mass and radius, we calculated a mean density of $\rho_b = 1.85^{+0.51}_{-0.44}$ g cm^{-3} (~28% precision).

Although the results obtained with `pyaneti` are robust, we performed a second joint analysis of the light curves and RVs with `juliet` (Espinoza et al. 2019) as a sanity check. The derived planetary parameters are consistent within errors with those presented in Sect. 4.4. The `juliet` planetary radius and mass are $R_b = 2.54 \pm 0.12\,R_\oplus$ (~5%), and $M_b = 5.7 \pm 1.1\,M_\oplus$ (~20%), respectively.

Table 3. TOI-4438 b parameters from the joint RVs and transit modeling with `pyaneti`.

Parameter	Prior	Derived value (e = 0)	Derived value ($e \neq 0$)
Model parameters			
$P_{\mathrm{orb,b}}$ (days)	$\mathcal{U}[7.2,7.7]$	7.44628 ± 0.000009	7.44628 ± 0.000009
$T_{0,\mathrm{b}}$ (BJD$_{\mathrm{TDB}}$$-2\,450\,000$)	$\mathcal{U}[9396.16, 9396.66]$	9396.41178 ± 0.00066	9396.41168 ± 0.00065
$R_{\mathrm{b}}/R_{\star}$	$\mathcal{U}[0.001,0.09]$	0.0613 ± 0.0007	0.062 ± 0.001
b_{b}	$\mathcal{U}[0,1]$	$0.18^{+0.15}_{-0.13}$	$0.39^{+0.16}_{-0.24}$
$\sqrt{e_{\mathrm{b}}}\sin\omega_{\star,\mathrm{b}}$	$\mathcal{U}[-1,1]$	0.0	$-0.31^{+0.20}_{-0.14}$
$\sqrt{e_{\mathrm{b}}}\cos\omega_{\star,\mathrm{b}}$	$\mathcal{U}[-1,1]$	0.0	$0.11^{+0.14}_{-0.19}$
K_{b} (m s^{-1})	$\mathcal{U}[0,50]$	3.23 ± 0.69	3.50 ± 0.72
Derived parameters			
M_{b} ($M_{\oplus}$)	...	5.1 ± 1.1	5.4 ± 1.1
R_{b} ($R_{\oplus}$)	...	2.48 ± 0.12	2.52 ± 0.13
ρ_{b} (g cm^{-3})	...	$1.80^{+0.53}_{-0.44}$	$1.85^{+0.51}_{-0.44}$
a_{b} (au)	...	0.0509 ± 0.0028	0.0534 ± 0.0037
e_{b}	...	0.0	0.14 ± 0.09
$\omega_{\star,\mathrm{b}}$ (deg)	...	0.0	-70^{+36}_{-32}
i_{b} (deg)	...	$89.64^{+0.25}_{-0.31}$	$89.34^{+0.39}_{-0.21}$
$\tau_{14,\mathrm{b}}$ (h)	...	2.002 ± 0.018	$2.021^{+0.033}_{-0.025}$
$T_{\mathrm{eq,b}}$ (K) (a=0)	...	446 ± 13	435 ± 15
$T_{\mathrm{eq,b}}$ (K) (a=0.6)	...	354 ± 7	347 ± 5
S_{b} ($S_{\oplus}$)	...	$6.57^{+0.81}_{-0.68}$	$6.00^{+0.90}_{-0.77}$
Additional model parameters			
$\rho_{\star}$ (g cm^{-3})	$\mathcal{N}[10.06,1.62]$	$8.92^{+0.49}_{-0.99}$	$10.1^{+1.7}_{-1.4}$
$\gamma_{\mathrm{CARMENES}}$ (m s^{-1})	$\mathcal{U}[-2,2]$	-0.2 ± 0.5	-0.3 ± 0.5
RV jitter term $\sigma_{\mathrm{RV,CARMENES}}$ (m s^{-1})	$\mathcal{J}[0,100]$	$1.48^{+0.72}_{-0.79}$	$1.33^{+0.71}_{-0.80}$
Phot. jitter term σ_{TESS}	$\mathcal{J}[0,100]$	0.000060 ± 0.000055	0.000060 ± 0.000055
Phot. jitter term $\sigma_{\mathrm{MuSCAT2}\,i'}$	$\mathcal{J}[0,100]$	0.00014 ± 0.00011	0.00013 ± 0.00011
Phot. jitter term $\sigma_{\mathrm{MuSCAT2}\,z_s}$	$\mathcal{J}[0,100]$	0.00018 ± 0.00016	0.00017 ± 0.00016

4.5. Tidal damping of the eccentricity and its consequences

We estimated the current eccentricity decay timescale of TOI-4438b adopting the model by Leconte et al. (2010). We assumed that its current value is $e = 0.14$, although its actually measured value is compatible with zero at the 2σ level. To apply the tidal model, we expressed the product of the constant tidal time lag Δt_{p}, adopted by Leconte et al. (2010), by the Love number of the planet $k_{2,\mathrm{p}}$:

$$k_{2,\mathrm{p}}\Delta t_{\mathrm{p}} = \frac{3}{2Q'_{\mathrm{p}}n}, \qquad (1)$$

where Q'_{p} is the modified tidal quality factor of the planet itself, $n = 2\pi/P$ is the orbit mean motion, and P the orbital period.

The rheology of mini-Neptune planets is unknown, thus we investigated two extreme cases. The former assumed $Q'_{\mathrm{p}} = 10^5$, which is comparable to the modified tidal quality factor of Uranus or Neptune as estimated by for example Tittemore & Wisdom (1990) and Ogilvie (2014), and is appropriate for a body where the dissipation of the tidal energy occurs in a fluid interior; the latter assumed that tides are mainly dissipated inside a rocky core encompassing the whole mass of the planet 5.4 $M_{\oplus}$, but having a radius of 1.3 $R_{\odot}$. This hypotetical core radius corresponds to the peak of the smallest radius component of the distribution of the transiting planets as observed by Kepler (Fulton et al. 2017). According to the model by Owen & Wu (2017) such a radius corresponds to the mean size of the bare core that remains after the gaseous envelope of a mini-Neptune has been removed by photoevaporation after the first few 100 Myr after its host star settled on the main sequence. In the latter case, we adopted $Q'_{\mathrm{p}} = 300$ as in the case of our Earth (Henning et al. 2009) and neglected the small mass and tidal dissipation in the fluid outer envelope of the planet in comparison with that in its rocky core.

The present eccentricity tidal decay timescale was found to be $\tau_{\mathrm{e}} \equiv |e/(\mathrm{d}e/\mathrm{d}t)| \sim 24$ Gyr in the former case, while $\tau_{\mathrm{e}} \sim 2$ Gyr in the latter case. We noted that tidal dissipation inside the star has a negligible effect on the evolution of the eccentricity because of the relatively large separation of the planet and its small mass. Our results on the eccentricity decay timescale are critically dependent on the Q'_{p} of the planet, and therefore, it is difficult to reach a conclusion on the possibility that the current eccentricity is primordial or is still excited, for example, by the gravitational perturbation of a distant companion or by other effects (see, e.g., Correia et al. 2020).

An interesting consequence of the eccentric orbit of TOI-4438b is its expected pseudosynchronization with the orbital motion, that is, its rotation is predicted to be faster than the orbital mean motion n because tides tend to synchronize its rotation with the orbital velocity at periastron where they are stronger. Using the formalism of Leconte et al. (2010), we predicted a rotation period of the planet of 6.7 days, that is, 1.12 times shorter than its orbital period. Such a state of

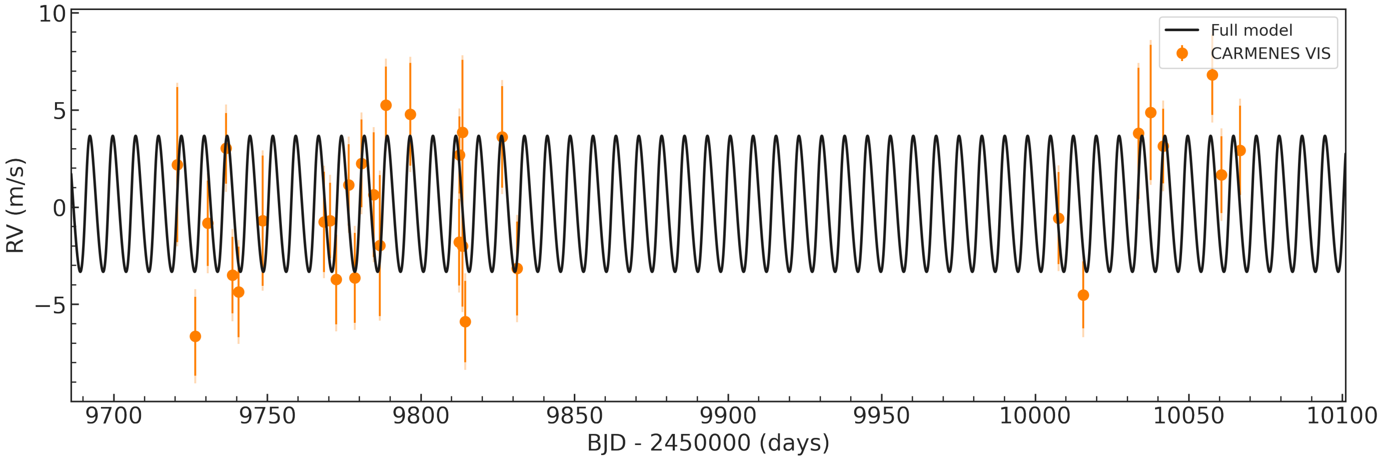

Fig. 10. CARMENES RV time series of TOI-4438 along with the best-fitting model. Data are shown as orange filled circles with their nominal uncertainties and semitransparent error bar extensions accounting for the jitter term.

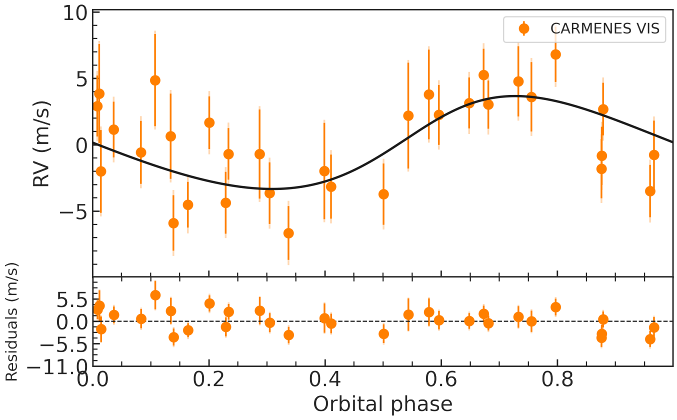

Fig. 11. Same as Fig. 10 but phase-folded at the orbital period of TOI-4438 b.

pseudosynchronization is reached after a timescale of ~0.26 Myr for $Q'_\mathrm{p} = 10^5$ or 5.6 kyr for $Q'_\mathrm{p} = 300$, that is, on timescales much shorter than the system lifetime. We expect tides to dissipate energy inside the planet due to its eccentric orbit and pseudosynchronous rotation. The maximum dissipated power is predicted for $Q'_\mathrm{p} = 300$ and is $\sim 6.3 \times 10^{16}$ W giving a heat flux of ~20 W m^{-2} at the top of its atmosphere with a radius of 2.5 $R_\oplus$. Such a flux is significantly larger than in the case of Jupiter, where the heat flux from the interior of the planet is ~5.4 W m^{-2} (Guillot et al. 2004). Therefore, it can play a relevant role in the atmospheric dynamics of the planet. On the other hand, adopting $Q'_\mathrm{p} = 10^5$, we found a dissipated power of 5.2×10^{15} W and a surface flux of only ~1.6 W m^{-2}.

5. Discussion

TOI-4438 b has a mass of $M_\mathrm{b} = 5.4 \pm 1.1\ M_\oplus$, and a radius of $R_\mathrm{b} = 2.52 \pm 0.13\ R_\oplus$, with precision of 20% and 5%, respectively. Its bulk density of $\rho_\mathrm{b} = 1.85^{+0.51}_{-0.44}$ g cm^{-3}, is close to Neptune's of 1.638 g cm^{-3} and 32% that of Earth's density. We calculated an equilibrium temperature of 435 K, assuming zero albedo. TOI-4438 b belongs to the small group ($\lesssim$50) of planets around M-dwarf stars whose masses and radii are known with a precision better than 25%. Figure 12 shows the mass–radius diagram with different theoretical composition models (Zeng et al. 2016). TOI-4438 b lies in the mini-Neptunes domain.

The position of TOI-4438 b in the mass-radius diagram is consistent with a high volatile content; it joins a group of low-density planets abundantly predicted in planet population syntheses based on the core accretion paradigm (e.g., Venturini et al. 2020; Burn et al. 2021; Schlecker et al. 2021a,b), where they correspond to planets with high (~50%) water ice mass fractions that accreted the bulk of their mass outside the water ice line (e.g., Mordasini 2018; Bitsch et al. 2021). However, the planet's bulk density is also compatible with an extended atmosphere.

With an instellation of $S_\mathrm{b} = 6.00^{+0.90}_{-0.77}\ S_\oplus$, TOI-4438 b is orbiting significantly closer to its host star than the predicted inner edge of the habitable zone (Kopparapu et al. 2014). As such, it may either have undergone an instellation-induced runaway greenhouse transition (e.g., Kasting 1988; Nakajima et al. 1992) and lost all its water to space, or currently be in a post-runaway state and host an extended steam atmosphere. The latter scenario is consistent with the planet's low bulk density (Turbet et al. 2020; Dorn & Lichtenberg 2021) and gains credibility through the expected long durations of runaway greenhouse phases in planets orbiting M dwarfs (Luger & Barnes 2015). With a derived instellation of a few times that of Earth, TOI-4438 b is well within the runaway greenhouse regime but close to the habitable zone inner edge. As such, and through the precise density estimate presented here, TOI-4438 b contributes to the currently small sample of planets suited to probe the habitable zone inner edge discontinuity, a predicted demographic imprint of the habitable zone inner edge in the radius–density distribution of small exoplanets (Turbet et al. 2019; Schlecker et al. 2024).

5.1. Interior modeling

Given the planet mass and radius obtained in our transit and radial velocity analyses, we derived the interior composition of TOI-4438 b. The forward model favoured an interior structure model for water-dominated sub-Neptunes (Acuña et al. 2021; Aguichine et al. 2021). The interior structure of the planet was assumed to consist of three layers: a Fe-rich core, a silicate mantle, and a water layer. The phases of water present in the top layer were determined self-consistently with the irradiation received by the planet from its host star and an atmospheric model. To compute the temperature in the deep water layer, we used the

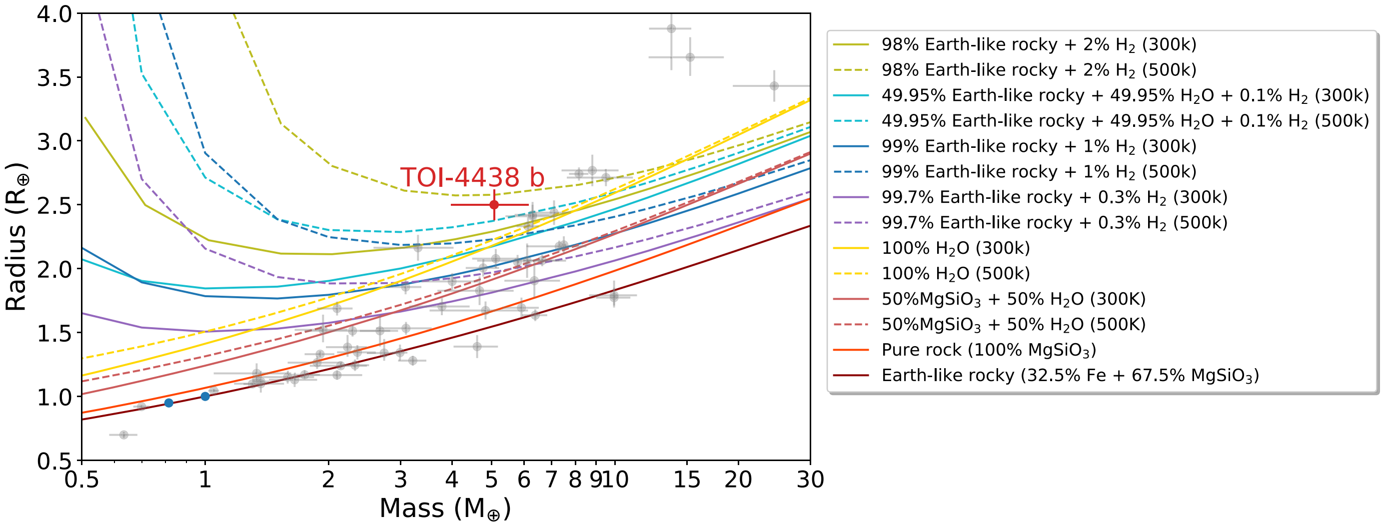

Fig. 12. Mass–radius diagram for well-characterized planets ($R < 4\,R_\oplus$, $M < 13\,M_\oplus$) around M-dwarf stars ($T_{\rm eff}$ <4000 K), as retrieved from the Transiting Extrasolar Planet Catalogue (Southworth 2011). The masses and radii are known with a precision better than 30% and 10%, respectively. The theoretical composition models from Zeng et al. (2019) are displayed from bottom to top, with solid and dashed curves. The location of TOI-4438 b is marked with a red dot.

k-correlated atmospheric model initially introduced in Marcq et al. (2017) and Pluriel et al. (2019), with up-to-date opacity and equation of state data from Acuña et al. (2023). The atmospheric model computed the temperature profile and the radius contribution of the upper water envelope (from 300 bar to 20 mbar). The interior and the atmospheric models were coupled self-consistently assuming radiative-convective equilibrium in the atmosphere, and with an iterative algorithm (Acuña et al. 2021). A water-dominated upper envelope was inferred with 99% H_2O and 1% CO_2.

TOI-4438 b's instellation is high enough to have molecules such as water in gas and supercritical phases. Figure 13 shows the posterior distribution functions of the free parameters in our interior composition retrieval. Due to the low density of the planet and its distance from the star, the refractory elements probably consist of silicates instead of a Si and Fe mixture (Aguichine et al. 2020). Therefore, in our analysis we set the Fe mass fraction to zero. We obtained a water mass fraction of $0.62^{+0.34}_{-0.16}$. With a composition between 46% and 96% H_2O (1σ), TOI-4438 b is volatile-rich. Moreover, it is very likely to have H/He atmosphere mixed with molecules, such as H_2O, CO_2, and CH_4. In the Solar System, comets and other small bodies with up to 80% of pure water have been found (McKay et al. 2019). However, low-mass planets with more than 50% water in mass are not a natural outcome of planetesimal accretion and other planet formation mechanisms (Kimura & Ikoma 2020; Miguel et al. 2020). Thus, atmospheric characterization is required to break the degeneracy between the mass and the composition of the envelope, and to determine whether TOI-4438 b has a massive, high metallicity envelope (i.e H_2O envelope scenario), or a less massive, low metallicity atmosphere (i.e. H/He-dominated envelope scenario).

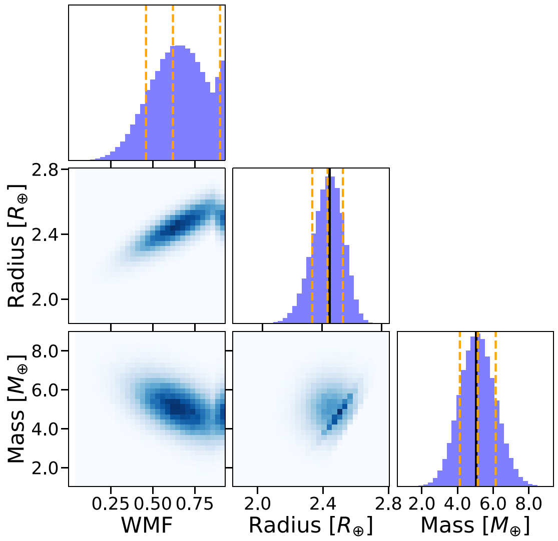

Fig. 13. Posterior probability distributions of the mass, radius and water mass fraction (WMF) derived from in the interior structure retrieval. The diagonal panels show the marginalized probability distributions of the individual parameters. For the observable parameters (mass and radius), the mean observed value is indicated with a black line. The mean and the 1σ interval of the posterior distributions retrieved in the MCMC are shown as orange dashed lines for all parameters. The PDFs agree well with the mean and uncertainties of the observed mass and radius.

5.2. Prospects for atmospheric characterization

We used the metric proposed by Kempton et al. (2018) to identify the transiting planets most amenable for atmospheric characterization via transmission spectroscopy with the JWST. For TOI-4438 b the derived transmission spectroscopy metric (TSM) is 136 ± 13, which is well above the threshold value of 92 defined for the respective planetary categories (small mini-Neptunes; $1.5\,R_\oplus < R_{\rm p} < 2.75\,R_\oplus$) for follow-up studies (Kempton et al. 2018). In this regard, TOI-4438 b is placed in the second quartile (rank 25–50%) of JWST targets with the strongest predicted atmospheric detections, and it is among the first five planets with the highest TSM, whose host stars have J-band magnitudes of 8.5 mag < J < 11.5 mag. Therefore, TOI-4438 b is one of the best small mini-Neptune targets for atmospheric characterization. Figure 14 shows the TSM value of TOI-4438 b along with the TSMs of known transiting planets smaller than $4\,R_\oplus$

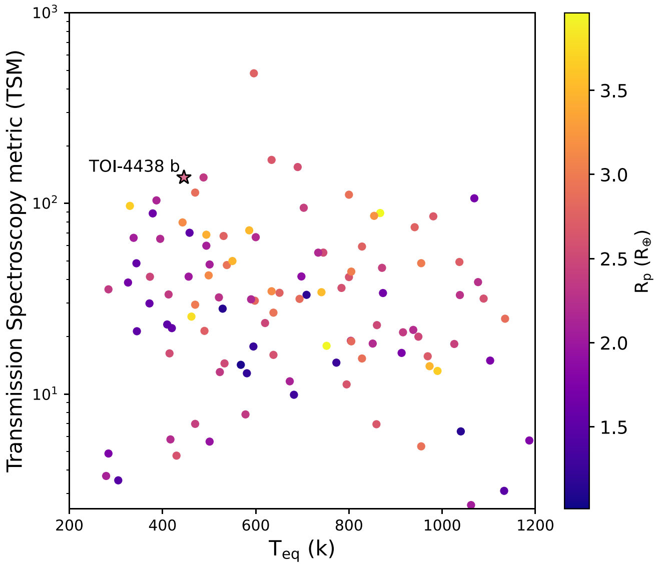

Fig. 14. TSM for planets with radii smaller than $4\,R_\oplus$ and measured masses, whose host stars have J-band magnitudes of $8.5\,\mathrm{mag} < J < 11.5\,\mathrm{mag}$. TOI-4438 b is displayed with a star symbol. The color indicates the radius of the planets.

with measured masses, as retrieved from the Transiting Extrasolar Planet Catalogue (Southworth 2011). We also calculated the emission spectroscopy metric (ESM) following Kempton et al. (2018) finding an ESM of ~4, which instead is below the suggested threshold value (i.e., ESM = 7.5). The planet TOI-4438 b is not a high priority target for emission spectroscopy of terrestrial planets with JWST.

We explored the potential of TOI-4438 b for transmission spectroscopy with the JWST through spectral simulations for a set of model atmospheres consistent with the planetary mass, radius, and equilibrium temperature. We adopted `TauREx 3` (Al-Refaie et al. 2021) to generate the synthetic transmission spectra. TOI-4438 b could have a rocky core surrounded by an H/He envelope or be a waterworld (Sect. 5.1). We modeled H/He atmospheres with 1× and 100× scaled solar abundances using the atmospheric chemical equilibrium module (Agúndez et al. 2012), including collisionally induced absorption by H_2–H_2 and H_2–He (Abel et al. 2011, 2012; Fletcher et al. 2018), and Rayleigh scattering. For each chemical setup, we considered the cases of clear and hazy atmospheres. The haze was modeled by Mie scattering with the formalism of Lee et al. (2013), assuming a particle size of $\alpha = 0.05$ µm, a mixing ratio of $\chi_c = 10^{-12}$, and an extinction coefficient of $Q_0 = 40$. While this assumption has some limitations in reproducing the actual behavior of scattered light due to using spherical particles instead of non-spherical ones (see, e.g., Mishchenko et al. 1996), this strategy was motivated by its low computational cost. The same haze parameters were chosen in previous atmospheric simulation studies (e.g. Orell-Miquel et al. 2023). We note that a super-solar metallicity is expected from planetary formation theories (e.g., Fortney et al. 2013; Thorngren et al. 2016). The equilibrium temperature within ~400–600 K also points to a high degree of haziness due to inefficient haze removal (Gao & Zhang 2020; Ohno & Tanaka 2021; Yu et al. 2021). Additionally, we modeled the case of a steam H_2O atmosphere.

We used `ExoTETHyS` (Morello et al. 2021) to simulate the corresponding JWST spectra, as observed with the NIRISS-SOSS (0.6–2.8 µm), NIRSpec-G395H (2.88–5.20 µm), and MIRI-LRS (5–12 µm) instrumental modes. The spectroscopic error bars obtained with `ExoTETHyS` are consistent with those calculated using the Exoplanet Characterization Toolkit (ExoCTK, Bourque et al. 2021) and `PandExo` (Batalha et al. 2017), as proven in previous studies (Murgas et al. 2021; Espinoza et al. 2022; Luque et al. 2022a,b; Chaturvedi et al. 2022; Lillo-Box et al. 2023; Orell-Miquel et al. 2023; Palle et al. 2023). We conservatively increased the error estimates by 20%. We chose the sizes of the wavelength bins following the recommendations from recent JWST data synthesis papers that adopted a spectral resolution of $R \sim 100$ for NIRISS and NIRSpec (Carter et al., Nat. Astron, accepted), and a constant bin size of 0.25 µm for MIRI-LRS observations (Powell et al. 2024).

Figure 15 shows the synthetic transmission spectra for the atmospheric configurations above. The H/He model atmospheres exhibit strong H_2O and CH_4 absorption features of $\gtrsim$100–1000 parts per million (ppm), depending on metallicity and haze, while the steam H_2O atmosphere has absorption features $\lesssim$100 ppm. The predicted error bars for a single transit observation are 31–123 ppm (mean error 53 ppm) for NIRISS-SOSS, 38–82 ppm (mean error 56 ppm) for NIRSpec-G395H, and 47–89 ppm (mean error 64 ppm) for MIRI-LRS. Our simulations suggest that a single transit observation with NIRISS-SOSS or NIRSpec-G395H is well suited to detect an H/He atmosphere, while at least two transit observations may be needed to reveal a secondary H_2O- dominated atmosphere.

5.3. Expected radio emission from star-planet interaction

Here we assess the feasibility of detecting radio emission arising from magnetic star–planet interaction (SPI) between TOI-4438b and its host star. The physical phenomenon responsible for this kind of emission is the electron cyclotron maser (ECM) instability (Melrose & Dulk 1982), which can generate auroral radio emission on the star and also the planet itself.

The characteristic frequency associated with ECM is given by the electron gyrofrequency, $\nu_G = 2.8\,B$ MHz, where B is the local magnetic field in Gauss. This non-thermal emission is coherent and circularly polarized (reaching up to 100% in some instances), and may reach a large bandwidth ($\Delta\nu \sim \nu_G/2$).

We note, however, that any kind of SPI emission coming from the planet itself would be undetectable with current instrumentation. The reason is that the magnetic field of a planet is merely a few Gauss, so the resulting emission would be blocked by the Earth's ionosphere. We therefore studied the auroral emission on the star TOI-4438 induced by the presence of its planet b, since the global magnetic field of the star is of the order of a few hundreds of Gauss or larger. As a result, the corresponding electron gyrofrequency would be of several hundreds or thousands of MHz, a frequency range that can be studied with current observatories. This phenomenon takes place in the sub-Alfvénic regime, that is, when the planet is close enough to the star that the speed of the plasma wind is lower than the Alfvén speed, enabling energy and momentum to travel back from the planet onto the star in the form of Alfvèn wings, triggering the radio emission close to the stellar surface.

To estimate the magnetic field of TOI-4438, we used the relation from Reiners et al. (2022), who estimated the Rossby number as a function of the stellar mass with the relations from Wright et al. (2018), which yields a value of $B_\star \approx 191.9$ G. We then used the code described in Pérez-Torres et al. (2021) to estimate the flux density arising from the sub-Alfvénic interaction between an exoplanet and its host star, for an isothermal wind.

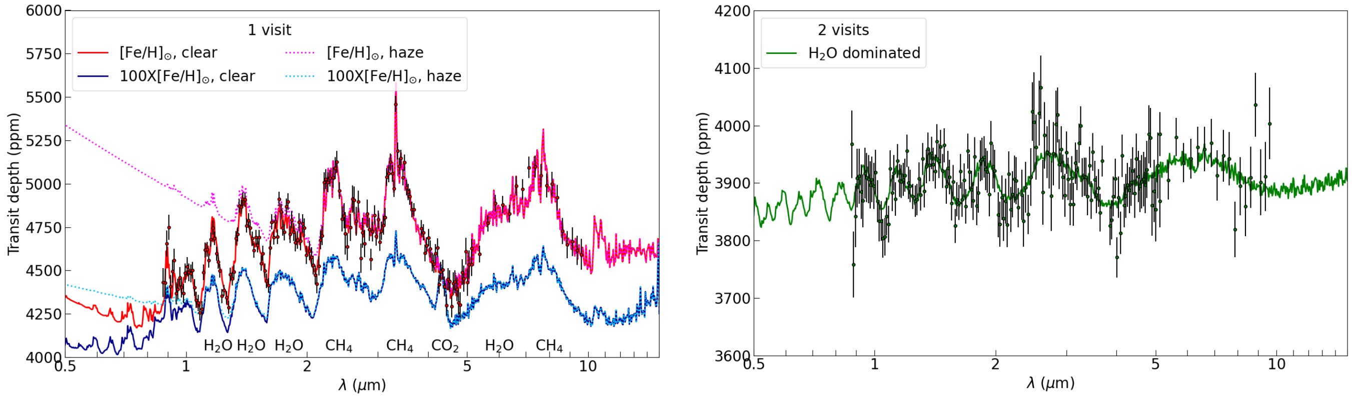

Fig. 15. Synthetic atmospheric transmission spectra of TOI-4438 b. *Left*: fiducial models for clear or hazy H/He atmospheres with scaled solar abundances. *Right*: model for a steam H_2O atmosphere. Simulated measurements with error bars are shown for the observation of one (*left*) or two (*right*) transits with JWST NIRISS-SOSS, NIRSpec-G395H, and MIRI-LRS configurations.

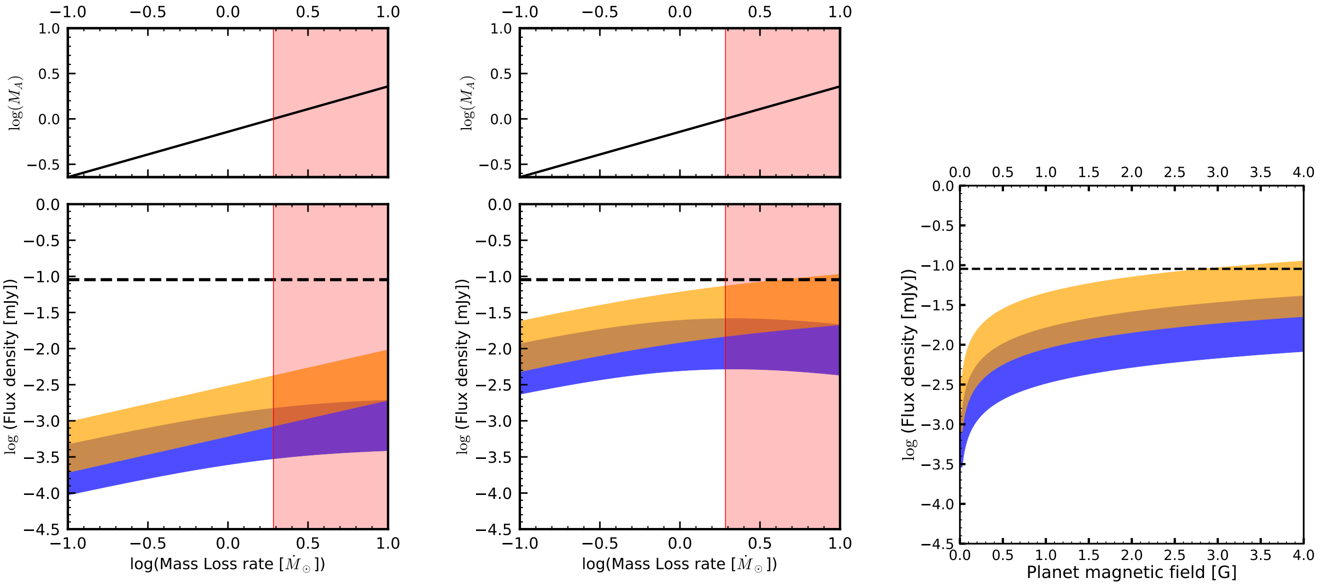

Fig. 16. Flux density arising from star planet interaction as a function of stellar mass-loss rate (*left* and *center*) and the magnetic field of the planet (*right*). The emission expected from Saur–Turnpenney's model is shown in orange, while the emission expected from Zarka–Lanza's model is shown in blue. The overlap between both models is shown in brown. We show in pale red color the region when the planet is in the super-Alfvènic regime. The dashed black line represents an assumed detection threshold of 100 μJy. For the variation with respect to the magnetic field of the planet we used $\dot{M} = 1.92\,\dot{M}_\odot$, which is the maximum value for the mass loss rate before entering the sub-Alfvènic regime. *Left*: expected flux density for an unmagnetized planet in a closed dipolar geometry, as a function of the stellar wind mass loss. The pale red colored region indicates the super-Alfvénic case, when our approach no longer applies. *Center*: the same as in the left panel, but for a magnetized planet with $B_\mathrm{p} = 2$ G. *Right*: expected flux density for a closed dipolar geometry

For our calculations, we assumed an isothermal wind with coronal temperature equal to that of the solar corona, $T = 2 \times 10^6$ K, and which is also adequate for M dwarf stars. We took the solid angle covered by the ECM emission to be 1.6 sterradians, in conformity with observations of the Jupiter-Io decametric radio emission (Ray & Hess 2008). We worked with two different emission models, Saur–Turnpenney (Saur et al. 2013; Turnpenney et al. 2018) and Zarka–Lanza (Zarka 2007; Lanza 2009), and in both cases we considered an efficiency in the conversion from Poynting flux to radio emission in the range from 0.2 to 1%.

In the left panels of Fig. 16, we show the radio flux density from sub-Alfvénic star–planet interaction as a function of the mass-loss rate of the star for an unmagnetized planet and a planet with a magnetic field of 2 G. In this regime, our approach does not apply and, therefore, no radio emission from SPI can reach us. In the right panel of Fig. 16 we show the emission as a function of the magnetic field of the planet. Despite the planet being rather large in size, the expected radio emission is too low to be detectable in essentially all scenarios due to the large distance to the system (30 pc). Only in the case when the planet is highly magnetized and the stellar wind is relatively powerful there could be marginal chances of detecting a signal from SPI.

6. Conclusions

We have reported the confirmation and characterization of TOI-4438 b, a mini-Neptune around an M3.5 V star (G 182-34) on a 7.44 days orbit. We performed a joint modeling of the TESS and MuSCAT2 light curves with CARMENES high-resolution spectroscopy measurements. We found a radius of 2.52 ± 0.13 $R_\oplus$ and a mass of 5.4 ± 1.1 $M_\oplus$, resulting in a bulk density of

$1.85^{+0.51}_{-0.44}$ g cm^{-3}. The equilibrium temperature of the planet is 435 ± 15 K.

Our interior structure retrieval with a pure water envelope yields a minimum water mass fraction of 46% (1σ). The volatile-rich mini-Neptune TOI-4438 b has likely H/He mixed with molecules, such as water, CO_2, and CH_4. TOI-4438 b presents a high transmission spectroscopy metric of 136 ± 13, which places the planet among the most suitable targets for atmospheric observations with JWST. We performed spectral simulations to explore the potential for transmission spectroscopy with JWST. A single transit observation of TOI-4438 with NIRISS-SOSS or NIRSpec-G395H should be adequate to detect an H/He atmosphere, while at least two transits may be needed to reveal a secondary H_2O dominated atmosphere.

Acknowledgements. We acknowledge the use of public TESS data from pipelines at the TESS Science Office and at the TESS Science Processing Operations Center. TESS data presented in this paper were obtained from the Milkulski Archive for Space Telescopes (MAST) at the Space Telescope Science Institute. Resources supporting this work were provided by the NASA High-End Computing (HEC) Program through the NASA Advanced Supercomputing (NAS) Division at Ames Research Center for the production of the SPOC data products. CARMENES is an instrument at the Centro Astronómico Hispano en Andalucía (CAHA) at Calar Alto (Almería, Spain), operated jointly by the Junta de Andalucía and the Instituto de Astrofísica de Andalucía (CSIC). CARMENES was funded by the Max-Planck-Gesellschaft (MPG), the Consejo Superior de Investigaciones Científicas (CSIC), the Ministerio de Economía y Competitividad (MINECO) and the European Regional Development Fund (ERDF) through projects FICTS-2011-02, ICTS-2017-07-CAHA-4, and CAHA16-CE-3978, and the members of the CARMENES Consortium (Max-Planck-Institut für Astronomie, Instituto de Astrofísica de Andalucía, Landessternwarte Königstuhl, Institut de Ciències de l'Espai, Institut für Astrophysik Göttingen, Universidad Complutense de Madrid, Thüringer Landessternwarte Tautenburg, Instituto de Astrofísica de Canarias, Hamburger Sternwarte, Centro de Astrobiología and Centro Astronómico Hispano-Alemán), with additional contributions by the MINECO, the Deutsche Forschungsgemeinschaft (DFG) through the Major Research Instrumentation Programme and Research Unit FOR2544 "Blue Planets around Red Stars", the Klaus Tschira Stiftung, the states of Baden-Württemberg and Niedersachsen, and by the Junta de Andalucía. The results reported herein benefitted from collaborations and/or information exchange within NASA's Nexus for Exoplanet System Science (NExSS) research coordination network sponsored by NASA's Science Mission Directorate under Agreement No. 80NSSC21K0593 for the program "Alien Earths". The *Joan Oró* Telescope (TJO) of the Montsec Observatory (OdM) is owned by the Catalan Government and operated by the Institute for Space Studies of Catalonia (IEEC). G.M. has received fundings from the Ariel Postdoctoral Fellowship program of the Swedish National Space Agency (SNSA). S.V.J. acknowledges the support of the DFG priority program SPP 1992 "Exploring the Diversity of Extrasolar Planets" (JE 701/5-1). M.P.T. and L.P.M. acknowledge financial support through grants CEX2021-001131-S and PID2020-117404GB-C21, funded by MCIU/AEI/10.13039/501100011033. L.P.M. also acknowledges funding through the grant PRE2020-095421, funded by MCIU/AEI/10.13039/501100011033 and by FSE Investing in your future. This work is partly supported by JSPS KAKENHI Grant Number JP18H05439, JST CREST Grant Number JPMJCR1761. This article is based on observations made with the MuSCAT2 instrument, developed by ABC, at Telescopio *Carlos Sánchez* operated on the island of Tenerife by the IAC in the Spanish Observatorio del Teide. We acknowledge financial support from the Agencia Estatal de Investigación (AEI/10.13039/501100011033) of the Ministerio de Ciencia e Innovación and the ERDF "A way of making Europe" through projects PID2022-137241NB-C4[1:4], PID2021-125627OB-C31, PID2019–109522GB–C5[1:4], and the Centre of Excellence "Severo Ochoa" and "María de Maeztu" awards to the Instituto de Astrofísica de Canarias (CEX2019-000920-S), Instituto de Astrofísica de Andalucía (CEX2021-001131-S) and Institut de Ciències de l'Espai (CEX2020-001058-M). This work was also funded by the Generalitat de Catalunya/CERCA programme, the DFG through grant HA3279/14-1 and the priority program SPP 1992 "Exploring the Diversity of Extrasolar Planets" (JE 701/5-1), the JSPS KAK-ENHI through grant JP18H05439, the JST CREST through grant JPMJCR1761, and the Israel Science Foundation through grant 1404/22.

References

Abel, M., Frommhold, L., Li, X., & Hunt, K. L. C. 2011, J. Phys. Chem. A, 115, 6805

Abel, M., Frommhold, L., Li, X., & Hunt, K. L. C. 2012, J. Chem. Phys., 136, 044319

Acuña, L., Deleuil, M., Mousis, O., et al. 2021, A&A, 647, A53

Acuña, L., Deleuil, M., & Mousis, O. 2023, A&A, 677, A14

Aguichine, A., Mousis, O., Devouard, B., & Ronnet, T. 2020, ApJ, 901, 97

Aguichine, A., Mousis, O., Deleuil, M., & Marcq, E. 2021, ApJ, 914, 84

Agúndez, M., Venot, O., Iro, N., et al. 2012, A&A, 548, A73

Al-Refaie, A. F., Changeat, Q., Waldmann, I. P., & Tinetti, G. 2021, ApJ, 917, 37

Aller, A., Lillo-Box, J., Jones, D., Miranda, L. F., & Barceló Forteza, S. 2020, A&A, 635, A128

Anderson, D. R., Cameron, A. C., Hellier, C., et al. 2010, ApJ, 726, L19

Baglin, A., Auvergne, M., Boisnard, L., et al. 2006, in 36th COSPAR Scientific Assembly, 36, 3749

Ballerini, P., Micela, G., Lanza, A. F., & Pagano, I. 2012, A&A, 539, A140

Barkaoui, K., Timmermans, M., Soubkiou, A., et al. 2023, A&A, 677, A38

Barragán, O., Gandolfi, D., & Antoniciello, G. 2019, MNRAS, 482, 1017

Barragán, O., Aigrain, S., Rajpaul, V. M., & Zicher, N. 2022, MNRAS, 509, 866

Batalha, N. M., Rowe, J. F., Bryson, S. T., et al. 2013, ApJS, 204, 24

Batalha, N. E., Mandell, A., Pontoppidan, K., et al. 2017, PASP, 129, 064501

Bayo, A., Rodrigo, C., Barrado Y Navascués, D., et al. 2008, A&A, 492, 277

Bitsch, B., Raymond, S. N., Buchhave, L. A., et al. 2021, A&A, 649, L5

Borucki, W. J., Koch, D., Basri, G., et al. 2010, Science, 327, 977

Bouma, L. G., Palumbo, E. K., & Hillenbrand, L. A. 2023, ApJ, 947, L3

Bourque, M., Espinoza, N., Filippazzo, J., et al. 2021, `https://doi.org/10.5281/zenodo.4556063`

Brown, T. M., Baliber, N., Bianco, F. B., et al. 2013, PASP, 125, 1031

Burn, R., Schlecker, M., Mordasini, C., et al. 2021, A&A, 656, A72

Caballero, J. A., Guàrdia, J., López del Fresno, M., et al. 2016, SPIE Conf. Ser., 9910, 99100E

Chaturvedi, P., Bluhm, P., Nagel, E., et al. 2022, A&A, 666, A155

Chen, G., Pallé, E., Parviainen, H., et al. 2021, MNRAS, 500, 5420

Cifuentes, C., Caballero, J. A., Cortés-Contreras, M., et al. 2020, A&A, 642, A115

Claret, A., Hauschildt, P. H., & Witte, S. 2012, A&A, 546, A14

Claret, A., Hauschildt, P. H., & Witte, S. 2013, A&A, 552, A16

Cochran, W. D., & Hatzes, A. P. 1996, Ap&SS, 241, 43

Collins, K. A., Kielkopf, J. F., Stassun, K. G., & Hessman, F. V. 2017, AJ, 153, 77

Colome, J., & Ribas, I. 2006, IAU Special Session, 6, 11

Colomé, J., Casteels, K., Ribas, I., & Francisco, X. 2010, SPIE Conf. Ser., 7740, 77403K

Correia, A. C. M., Bourrier, V., & Delisle, J. B. 2020, A&A, 635, A37

Cracchiolo, G., Micela, G., Morello, G., & Peres, G. 2021, MNRAS, 507, 6118

Curtis, J. L., Agüeros, M. A., Matt, S. P., et al. 2020, ApJ, 904, 140

Dahn, C. C., Harrington, R. S., Kallarakal, V. V., et al. 1988, AJ, 95, 237

Dahn, C. C., Harris, H. C., Vrba, F. J., et al. 2002, AJ, 124, 1170

Delrez, L., Murray, C. A., Pozuelos, F. J., et al. 2022, A&A, 667, A59

Dévora-Pajares, M., & Pozuelos, F. J. 2022, `https://doi.org/10.5281/zenodo.6570832`

Dorn, C., & Lichtenberg, T. 2021, ApJ, 922, L4

Dressing, C. D., & Charbonneau, D. 2013, ApJ, 767, 95

Engle, S. G., & Guinan, E. F. 2023, ApJ, 954, L50

Espinoza, N., Kossakowski, D., & Brahm, R. 2019, MNRAS, 490, 2262

Espinoza, N., Pallé, E., Kemmer, J., et al. 2022, AJ, 163, 133

Fletcher, L. N., Gustafsson, M., & Orton, G. S. 2018, ApJS, 235, 24

Foreman-Mackey, D. 2016, J. Open Source Softw., 1, 24

Foreman-Mackey, D., Hogg, D. W., Lang, D., & Goodman, J. 2013, PASP, 125, 306

Fortney, J. J., Mordasini, C., Nettelmann, N., et al. 2013, ApJ, 775, 80

Frith, J., Pinfield, D. J., Jones, H. R. A., et al. 2013, MNRAS, 435, 2161

Fulton, B. J., Petigura, E. A., Howard, A. W., et al. 2017, AJ, 154, 109

Gaia Collaboration (Smart, R. L., et al.) 2021, A&A, 649, A6

Gaia Collaboration (Vallenari, A., et al.) 2023, A&A, 674, A1

Gao, P., & Zhang, X. 2020, ApJ, 890, 93

Giclas, H. 1966, Vistas Astron., 8, 23

Giclas, H. L., Burnham, R., & Thomas, N. G. 1971, Lowell proper motion survey Northern Hemisphere. The G numbered stars. 8991 stars fainter than magnitude 8 with motions > 0″.26/year (Flagstaff, Arizona: Lowell Observatory)

González-Álvarez, E., Zapatero Osorio, M. R., Caballero, J. A., et al. 2023, A&A, 675, A177

Guillot, T., Stevenson, D. J., Hubbard, W. B., & Saumon, D. 2004, in Jupiter. The Planet, Satellites and Magnetosphere, eds. F. Bagenal, T. E. Dowling, & W. B. McKinnon (Cambridge University Press), 35

Hartman, J. D., & Bakos, G. Á. 2016, Astron. Comput., 17, 1

Hatzes, A. P. 2019, The Doppler Method for the Detection of Exoplanets (Bristol, UK: IOP Publishing)

Hatzes, A. P., Dvorak, R., Wuchterl, G., et al. 2010, A&A, 520, A93

Henning, W. G., O'Connell, R. J., & Sasselov, D. D. 2009, ApJ, 707, 1000

Howell, S. B., Sobeck, C., Haas, M., et al. 2014, PASP, 126, 398

Husser, T. O., Wende-von Berg, S., Dreizler, S., et al. 2013, A&A, 553, A6

Jeffers, S. V., Schöfer, P., Lamert, A., et al. 2018, A&A, 614, A76

Jeffers, S. V., Dreizler, S., Barnes, J. R., et al. 2020, Science, 368, 1477

Jenkins, J. M., Twicken, J. D., McCauliff, S., et al. 2016, Proc. SPIE, 9913, 99133E

Kasting, J. F. 1988, Icarus, 74, 472

Kawauchi, K., Murgas, F., Palle, E., et al. 2022, A&A, 666, A4

Kempton, E. M. R., Bean, J. L., Louie, D. R., et al. 2018, PASP, 130, 114401

Kimura, T., & Ikoma, M. 2020, MNRAS, 496, 3755

Kipping, D. M. 2013, MNRAS, 435, 2152

Kochanek, C. S., Shappee, B. J., Stanek, K. Z., et al. 2017, PASP, 129, 104502

Kopparapu, R. K., Ramirez, R. M., SchottelKotte, J., et al. 2014, ApJ, 787, L29

Kossakowski, D., Kürster, M., Trifonov, T., et al. 2023, A&A, 670, A84

Kovács, G., Zucker, S., & Mazeh, T. 2002, A&A, 391, 369

Lamman, C., Baranec, C., Berta-Thompson, Z. K., et al. 2020, AJ, 159, 139

Lanza, A. F. 2009, A&A, 505, 339

Leconte, J., Chabrier, G., Baraffe, I., & Levrard, B. 2010, A&A, 516, A64

Lee, J.-M., Heng, K., & Irwin, P. G. J. 2013, ApJ, 778, 97

Lépine, S., & Gaidos, E. 2011, AJ, 142, 138

Lépine, S., & Shara, M. M. 2005, AJ, 129, 1483

Lillo-Box, J., Gandolfi, D., Armstrong, D. J., et al. 2023, A&A, 669, A109

Lodieu, N., Pérez-Garrido, A., Smart, R. L., & Silvotti, R. 2019, A&A, 628, A66

Luger, R., & Barnes, R. 2015, Astrobiology, 15, 119

Luque, R., Fulton, B. J., Kunimoto, M., et al. 2022a, A&A, 664, A199

Luque, R., Nowak, G., Hirano, T., et al. 2022b, A&A, 666, A154

Luyten, W. J. 1979, LHS catalogue. A catalogue of stars with proper motions exceeding 0”5 annually, 2nd edn (Minneapolis: University of Minnesota)

Mallorquín, M., Goffo, E., Pallé, E., et al. 2023, A&A, 680, A76

Mandel, K., & Agol, E. 2002, ApJ, 580, L171

Marcq, E., Salvador, A., Massol, H., & Davaille, A. 2017, J. Geophys. Res. (Planets), 122, 1539

Marfil, E., Tabernero, H. M., Montes, D., et al. 2021, A&A, 656, A162

Maxted, P. F. L., Anderson, D. R., Collier Cameron, A., et al. 2011, PASP, 123, 547

McCully, C., Volgenau, N. H., Harbeck, D.-R., et al. 2018, SPIE Conf. Ser., 10707, 107070K

McKay, A. J., DiSanti, M. A., Kelley, M. S. P., et al. 2019, AJ, 158, 128

Melrose, D. B., & Dulk, G. A. 1982, ApJ, 259, 844

Miguel, Y., Cridland, A., Ormel, C. W., Fortney, J. J., & Ida, S. 2020, MNRAS, 491, 1998

Mishchenko, M. I., Travis, L. D., & Mackowski, D. W. 1996, J. Quant. Spec. Radiat. Transf., 55, 535

Mordasini, C. 2018, in Handbook of Exoplanets (Cham: Springer International Publishing), 2425

Morello, G., Tsiaras, A., Howarth, I. D., & Homeier, D. 2017, AJ, 154, 111

Morello, G., Zingales, T., Martin-Lagarde, M., Gastaud, R., & Lagage, P.-O. 2021, AJ, 161, 174

Morello, G., Parviainen, H., Murgas, F., et al. 2023, A&A, 673, A32

Murdoch, K. A., Hearnshaw, J. B., & Clark, M. 1993, ApJ, 413, 349

Murgas, F., Astudillo-Defru, N., Bonfils, X., et al. 2021, A&A, 653, A60

Murgas, F., Castro-González, A., Pallé, E., et al. 2023, A&A, 677, A182

Nagel, E., Czesla, S., Kaminski, A., et al. 2023, A&A, 680, A73

Nakajima, S., Hayashi, Y.-Y., & Abe, Y. 1992, J. Atmos. Sci., 49, 2256

Narita, N., Fukui, A., Kusakabe, N., et al. 2019, J. Astron. Telesc. Instrum. Syst., 5, 015001

Ogilvie, G. I. 2014, ARA&A, 52, 171

Ohno, K., & Tanaka, Y. A. 2021, ApJ, 920, 124

Orell-Miquel, J., Nowak, G., Murgas, F., et al. 2023, A&A, 669, A40

Osborne, H. L. M., Van Eylen, V., Goffo, E., et al. 2024, MNRAS, 527, 11138

Owen, J. E., & Wu, Y. 2017, ApJ, 847, 29

Palle, E., Orell-Miquel, J., Brady, M., et al. 2023, A&A, 678, A80

Parviainen, H. 2015, MNRAS, 450, 3233

Parviainen, H., & Aigrain, S. 2015, MNRAS, 453, 3821

Parviainen, H., Tingley, B., Deeg, H. J., et al. 2019, A&A, 630, A89

Pecaut, M. J., & Mamajek, E. E. 2013, ApJS, 208, 9

Pérez-Torres, M., Gómez, J. F., Ortiz, J. L., et al. 2021, A&A, 645, A77

Pluriel, W., Marcq, E., & Turbet, M. 2019, Icarus, 317, 583

Pollacco, D. L., Skillen, I., Collier Cameron, A., et al. 2006, PASP, 118, 1407

Powell, D., Feinstein, A. D., Lee, E. K. H., et al. 2024, Nature, 626, 979

Pozuelos, F. J., Suárez, J. C., de Elía, G. C., et al. 2020, A&A, 641, A23

Pozuelos, F. J., Timmermans, M., Rackham, B. V., et al. 2023, A&A, 672, A70

Quirrenbach, A., Amado, P. J., Caballero, J. A., et al. 2014, Proc. SPIE, 9147, 91471F

Quirrenbach, A., Amado, P. J., Ribas, I., et al. 2018, SPIE Conf. Ser., 10702, 107020W

Ray, L. C., & Hess, S. 2008, J. Geophys. Res. (Space Phys.), 113, A11218

Reid, I. N., & Cruz, K. L. 2002, AJ, 123, 2806

Reid, I. N., Cruz, K. L., Allen, P., et al. 2003, AJ, 126, 3007

Reiners, A., Shulyak, D., Käpylä, P. J., et al. 2022, A&A, 662, A41

Ribas, I., Reiners, A., Zechmeister, M., et al. 2023, A&A, 670, A139

Ricker, G. R., Winn, J. N., Vanderspek, R., et al. 2015, J. Astron. Telesc. Instrum. Syst., 1, 014003

Sabotta, S., Schlecker, M., Chaturvedi, P., et al. 2021, A&A, 653, A114

Saur, J., Grambusch, T., Duling, S., Neubauer, F. M., & Simon, S. 2013, A&A, 552, A119

Schanche, N., Pozuelos, F. J., Günther, M. N., et al. 2022, A&A, 657, A45

Schlecker, M., Mordasini, C., Emsenhuber, A., et al. 2021a, A&A, 656, A71

Schlecker, M., Pham, D., Burn, R., et al. 2021b, A&A, 656, A73

Schlecker, M., Apai, D., Lichtenberg, T., et al. 2024, Planet. Sci. J., 5, 3

Schneider, A. C., Greco, J., Cushing, M. C., et al. 2016, ApJ, 817, 112

Schöfer, P., Jeffers, S. V., Reiners, A., et al. 2019, A&A, 623, A44

Schweitzer, A., Passegger, V. M., Cifuentes, C., et al. 2019, A&A, 625, A68

Shappee, B. J., Prieto, J. L., Grupe, D., et al. 2014, ApJ, 788, 48

Skrutskie, M. F., Cutri, R. M., Stiening, R., et al. 2006, AJ, 131, 1163

Smith, J. C., Stumpe, M. C., Van Cleve, J. E., et al. 2012, PASP, 124, 1000

Southworth, J. 2011, MNRAS, 417, 2166

Stassun, K. G., Oelkers, R. J., Paegert, M., et al. 2019, AJ, 158, 138

Stumpe, M. C., Smith, J. C., Van Cleve, J. E., et al. 2012, PASP, 124, 985

Stumpe, M. C., Smith, J. C., Catanzarite, J. H., et al. 2014, PASP, 126, 100

Tabernero, H. M., Marfil, E., Montes, D., & González Hernández, J. I. 2022, A&A, 657, A66

Thompson, A., Biagini, A., Cracchiolo, G., et al. 2023, ApJ, accepted [arXiv:2302.04574]

Thorngren, D. P., Fortney, J. J., Murray-Clay, R. A., & Lopez, E. D. 2016, ApJ, 831, 64

Tittemore, W. C., & Wisdom, J. 1990, Icarus, 85, 394

Turbet, M., Ehrenreich, D., Lovis, C., Bolmont, E., & Fauchez, T. 2019, A&A, 628, A12

Turbet, M., Bolmont, E., Ehrenreich, D., et al. 2020, A&A, 638, A41

Turnpenney, S., Nichols, J. D., Wynn, G. A., & Burleigh, M. R. 2018, ApJ, 854, 72

van Altena, W. F., Lee, J. T., & Hoffleit, E. D. 1995, The general catalogue of trigonometric [stellar] parallaxes (New Haven, CT: Yale University Observatory)

Venturini, J., Guilera, O. M., Haldemann, J., Ronco, M. P., & Mordasini, C. 2020, A&A, 643, L1

Wells, R. D., Rackham, B. V., Schanche, N., et al. 2021, A&A, 653, A97

Wright, N. J., Newton, E. R., Williams, P. K. G., Drake, J. J., & Yadav, R. K. 2018, MNRAS, 479, 2351

Yu, X., He, C., Zhang, X., et al. 2021, Nat. Astron., 5, 822

Zarka, P. 2007, Planet. Space Sci., 55, 598

Zechmeister, M., & Kürster, M. 2009, A&A, 496, 577

Zechmeister, M., Anglada-Escudé, G., & Reiners, A. 2014, A&A, 561, A59

Zechmeister, M., Reiners, A., Amado, P. J., et al. 2018, A&A, 609, A12

Zeng, L., Sasselov, D. D., & Jacobsen, S. B. 2016, ApJ, 819, 127

Zeng, L., Jacobsen, S. B., Sasselov, D. D., et al. 2019, PNAS, 116, 9723

---

[1] Dipartimento di Fisica, Università degli Studi di Torino, via Pietro Giuria 1, 10125 Torino, Italy

[2] Thüringer Landessternwarte Tautenburg, 07778 Tautenburg, Germany
e-mail: `elisa@tls-tautenburg.de`

[3] Instituto de Astrofísica de Canarias (IAC), Calle Vía Láctea s/n, 38205 La Laguna, Tenerife, Spain

[4] Departamento de Astrofísica, Universidad de La Laguna (ULL), 38206 La Laguna, Tenerife, Spain

[5] Department of Space, Earth and Environment, Chalmers University of Technology, 412 96 Gothenburg, Sweden

[6] Max-Planck-Institut für Astronomie, Königstuhl 17, 69117 Heidelberg, Germany

[7] Instituto de Astrofísica de Andalucía (IAA-CSIC), Glorieta de la Astronomía s/n, 18008 Granada, Spain

[8] INAF – Osservatorio Astrofisico di Catania, Via S. Sofia 78, 95123 Catania, Italy
[9] Centro de Astrobiología, (CSIC-INTA), ESAC Campus, Camino bajo del castillo s/n, 28692 Villanueva de la Cañada, Madrid, Spain
[10] Steward Observatory and Department of Astronomy, The University of Arizona, Tucson, AZ 85721, USA
[11] Hamburger Sternwarte, Gojenbergsweg 112, 21029 Hamburg, Germany
[12] Astrophysics Group, Keele University, Staffordshire ST5 5BG, UK
[13] Max Planck Institut für Sonnensystemforschung, Justus-von-Liebig-Weg 3, 37077 Göttingen, Germany
[14] Departamento de Física de la Tierra y Astrofísica and IPARCOS-UCM (Instituto de Física de Partículas y del Cosmos de la UCM), Facultad de Ciencias Físicas, Universidad Complutense de Madrid, 28040 Madrid, Spain
[15] Department of Physics, Ariel University, Ariel 40700, Israel
[16] Vereniging Voor Sterrenkunde, Oude Bleken 12, 2400 Mol, Belgium
[17] AstroLAB IRIS, Provinciaal Domein “De Palingbeek”, Verbrandemolenstraat 5, 8902 Zillebeke, Ieper, Belgium
[18] Komaba Institute for Science, The University of Tokyo, 3-8-1 Komaba, Meguro, Tokyo 153-8902, Japan
[19] Department of Multi-Disciplinary Sciences, Graduate School of Arts and Sciences, The University of Tokyo, 3-8-1 Komaba, Meguro, Tokyo 153-8902, Japan
[20] Institut d’Estudis Espacials de Catalunya (IEEC), Calle Gran Capita 2–4, 08034 Barcelona, Spain
[21] Astrobiology Center, 2-21-1 Osawa, Mitaka, Tokyo 181-8588, Japan
[22] Centre for Mathematical Plasma-Astrophysics, Department of Mathematics, KU Leuven, Celestijnenlaan 200B, 3001 Heverlee, Belgium
[23] Centro Astronómico Hispano en Andalucía (CAHA), Observatorio de Calar Alto, Sierra de los Filabres, 04550 Gérgal, Spain
[24] Institut für Astrophysik und Geophysik, Georg-August-Universität Göttingen, Friedrich-Hund-Platz 1, 37077 Göttingen, Germany
[25] Department of Astronomy & Astrophysics, University of Chicago, Chicago, IL 60637, USA
[26] Landessternwarte, Zentrum für Astronomie der Universität Heidelberg, Königstuhl 12, 69117 Heidelberg, Germany
[27] Institut de Ciéncies de l’Espai (CSIC-IEEC), Campus UAB, de Can Magrans s/n, 08193 Bellaterra, Barcelona, Spain
[28] Centro de Astrobiología (CSIC-INTA), Carretera de Ajalvir km 4, 28850 Torrejón de Ardoz, Madrid, Spain
[29] Center for Astroparticles and High Energy Physics (CAPA), Universidad de Zaragoza, 50009 Zaragoza, Spain
[30] School of Sciences, European University Cyprus, Diogenes street, Engomi, 1516 Nicosia, Cyprus

Appendix A: Radial velocity data

Table A.1: RV data from CARMENES VIS.

Time [BJD$_{\mathrm{TDB}}$]	RV [m s^{-1}]	σ [m s^{-1}]
2459720.6490	1.90	3.99
2459726.5607	–6.93	2.02
2459730.5751	–1.11	2.20
2459736.5664	2.74	1.81
2459738.6403	–3.77	1.97
2459740.6490	–4.64	2.32
2459748.5283	–0.98	3.35
2459768.4734	–1.05	2.57
2459770.4685	–0.97	1.94
2459772.4574	–4.01	2.31
2459776.4443	0.86	2.09
2459778.4424	–3.92	2.31
2459780.6099	1.97	2.25
2459784.6203	0.36	3.21
2459786.5898	–2.26	3.63
2459788.6297	4.97	1.98
2459796.5221	4.49	2.64
2459812.4809	–2.08	2.23
2459812.5016	2.40	1.98
2459813.4895	3.57	3.72
2459813.5105	–2.29	3.12
2459814.4412	–6.17	2.09
2459826.4745	3.32	2.61
2459831.3528	–3.44	2.42
2460007.6296	–0.85	2.37
2460015.6770	–4.80	1.72
2460033.6556	3.51	3.38
2460037.5939	4.58	3.48
2460041.6186	2.86	1.92
2460057.6177	6.53	2.07
2460060.6283	1.38	1.98
2460066.6401	2.64	2.30

Appendix B: Photometric fit with unocculted star spots

We fitted the color dependent transit depths that appear when considering the measurements from TESS and all MuSCAT2 filters, including g' and r', following the method described in Sect. 4.1. For simplicity, we fixed the stellar parameters of the quiet photosphere to those of TOI-4438, as reported in Table 1. The free parameters in our fit were the geometric radius ratio $R_b/R_\star$, the star spot photospheric parameters T_{spot} and $\log g_{\mathrm{spot}}$, and filling factor f_{spot}. We run `emcee` (Foreman-Mackey et al. 2013) with 16 walkers and 30 000 iterations to sample the posterior distribution, then applying a conservative burn-in of 10 000 iterations, which is more than 20 times the maximum autocorrelation length. For each parameters set from the chains, we also computed the apparent transit depth in each passband using the formulae from Ballerini et al. (2012).

Fig. B.1 compares the measured transit depths in each passband with those derived from the fit with unocculted star spots and the posterior distribution for the model parameters. While the unocculted star spots may explain the larger transit depths in g' and r', they would also cause a difference between the i' and z_s that is not seen in the data. As a compromise, the model tends to underestimate the g' and r' transit depths to keep a small difference between i' and z_s. The modelled transit depths are consistent within 1σ with the measured ones, owing to the large error bars in g' and r'. The spot temperature contrast is -490^{+380}_{-640} K and the filling factor is $0.44^{+0.24}_{-0.17}$. In this scenario, the planet-to-star radius ratio is $R_b/R_\star = 0.055^{+0.004}_{-0.011}$, that is significantly smaller and with order-of-magnitude larger error bars than those obtained discarding the g' and r' bands and neglecting star spots.

If we accepted this solution, the planetary radius would be $R_b = 2.24^{+0.28}_{-0.55}\,R_\oplus$. This slightly smaller radius would not significantly change the predicted composition, which is volatile-rich. With a smaller TSM of 96, TOI-4438 b would remain a top target for atmospheric characterization with JWST.

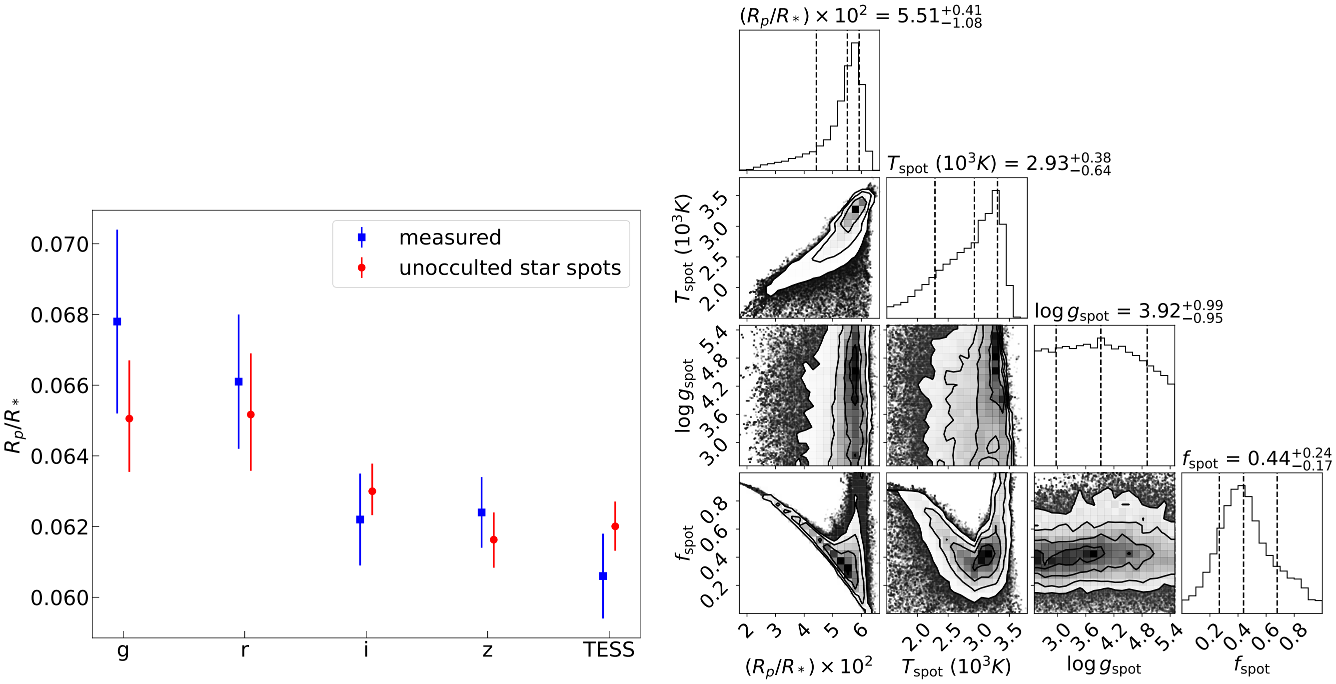

Fig. B.1: Results of the photometric fit with unocculted star spots. *Left*: Individual transit depths derived from photometric observations (blue squares) and best-fit model assuming that the color-dependence is due to unocculted star spots. *Right*: corner plot with the posterior distribution of the model parameters, generated with the `corner` package (Foreman-Mackey 2016).